2020

Experimental And Computational Studies Of Heat Transfer In Flexible Two-Dimensional Woven Fiber Ceramic Materials

Rodrigo Penide Fernandez
University of Vermont

EXPERIMENTAL AND COMPUTATIONAL STUDIES OF HEAT TRANSFER IN FLEXIBLE TWO-DIMENSIONAL WOVEN FIBER CERAMIC MATERIALS.

A Dissertation Presented

by

Rodrigo Penide Fernandez

to

The Faculty of the Graduate College

of

The University of Vermont

In Partial Fulfillment of the Requirements
For the Degree of Doctor of Philosophy
Specializing in Mechanical Engineering

October, 2020

Defense Date: September 10th, 2020
Dissertation Examination Committee:

Frederic Sansoz, PhD., Advisor
Ting Tan, Ph.D., Chairperson
Dryver Huston, Ph.D.
Niccolo Fiorentino, Ph.D.
Yves Dubief, Ph.D.
Cynthia J. Forehand, Ph.D., Dean of the Graduate College

ABSTRACT

Flexible thermal protection materials made from two-dimensional woven ceramics fibers are of significant interest for hypersonic inflatable aerodynamic decelerators being developed by NASA for future missions on Mars and other planets. A key component of the thermal shield is a heat-resistant outer ceramic fabric that must withstand harsh aero-thermal atmospheric entry conditions. However, a predictive understanding of heat conduction processes in complex woven-fiber ceramic materials under deformation is currently lacking. This dissertation presents a combined experimental and computational study of thermal conductivity in alumina-based Nextel-440 and silicon carbide Hi-Nicalon 5-harness-satin woven fabrics, using the hot-disk transient plane source method and computational multiscale thermo-mechanical modeling by finite-element analysis. The objective is to create a physics-based model for the anisotropic heat conduction in flexible two-dimensional ceramic materials and quantify and understand the effect of deformation and gas pressure over the out-of-plane thermal conductivity. We find, both experimentally and theoretically, that thermal conductivity of woven fabrics rises in both in-plane and out-of-plane directions, as the transverse load increases. Air gap conduction is shown to play a major role in the insulation capabilities of these materials. The proposed modeling methodology accurately captures the experimental heat conduction results and should be applicable to more complex loading conditions and different woven fabric materials, relevant to extreme high temperature environments.

CITATIONS

Material from this dissertation has been published in the following form:

R. Penide-Fernandez, F. Sansoz.. Anisotropic thermal conductivity under compression in two-dimensional woven ceramic fibers for flexible thermal protection systems. Int. J. Heat Mass Transf. 145 (2019) 118721.

ACKNOWLEDGEMENTS

Firstly, I would like to thank my advisor, Dr. Frederic Sansoz. For all the guidance and support I received through these years and for believing in me, I will be forever grateful. Special thanks to my dissertation committee members, Drs. Tan, Huston, Fiorentino, and Dubief for their help and confidence. Thanks to Cory, Zhiliang, Xing, Lily and Selina for the support I received from them and all the helpful discussions along the way. I am also grateful for all the help and support received from the staff in OIE and CEMS, each and every person working there has been exceptionally helpful.

Thanks to my family for the financial and emotional support, it is because of them that I have been able to get here. Thanks to all my friends for always being there for me, I could not ask for better people in my life.

Finally, this research was sponsored by the NASA EPSCoR Program under NASA Cooperative Agreement No. NNX14AN20A and No. NNX15AK55A together with graduate teaching assistantships from the UVM Mechanical Engineering department, to which I am grateful for the support.

TABLE OF CONTENTS

Page

LIST OF FIGURES

CHAPTER 1: INTRODUCTION

1.1 Flexible Thermal Protection Systems

Current Entry, Decent and Landing (EDL) systems are expected to face important challenges with the increasing landed payload weight and size in future space missions. Deployable aeroshells like the Hypersonic Inflatable Aerodynamic Decelerator (HIAD) have been proposed to overcome such challenges. The larger drag area attainable with this system (Figure 1.1(a)) can significantly reduce ballistic coefficients and afford higher Mach numbers and dynamic pressures. Despite the lower entry heating produced by a lower ballistic coefficient, hypersonic atmospheric entry still produces considerable aerothermal loads for the aeroshell to require a flexible Thermal Protection System (TPS) [1, 2].

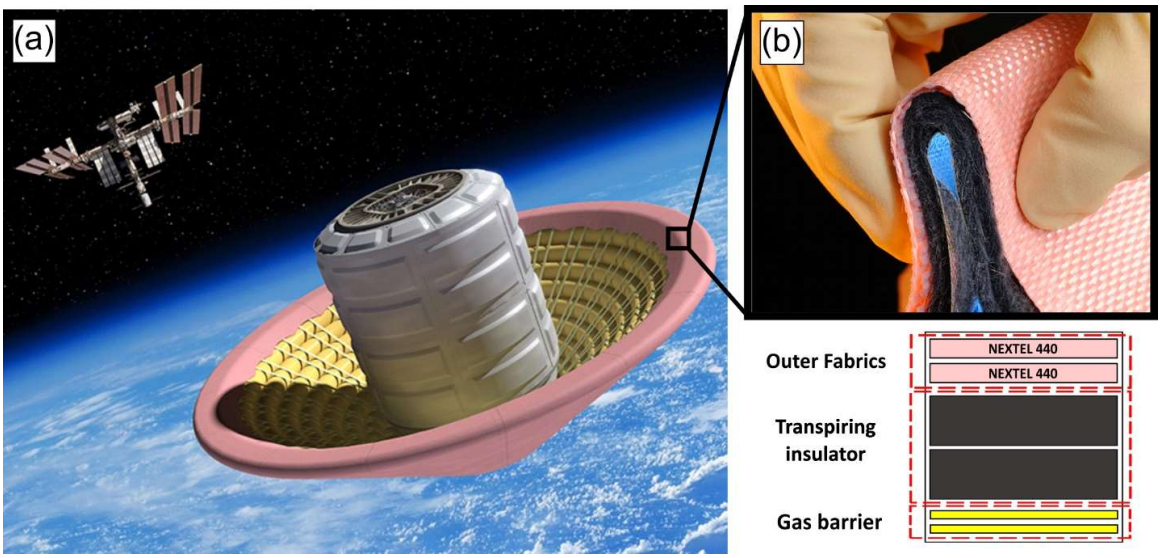

Figure 1.1: (a) Hypersonic Inflatable Aerodynamic Decelerator (HIAD). (b) Flexible thermal protection system lay-up structure. [modified NASA images]

Flexible TPSs consist of a lay-up structure of flexible insulating materials (Figure 1.1(b)), a typical configuration has: a set of two high temperature woven ceramic fabrics, that are exposed directly to atmospheric entry environments, to act as a heat-resistant ablative insulator. Two insulation layers to manage the heat load, typically high-temperature flexible aerogels. Finally, a laminated gas barrier to minimize hot gas inflow to the aeroshell structure, usually Kapton polyimide film [3].

Since the outer fabrics of the flexible thermal protection system are in direct contact with the hypersonic atmospheric entry flow, a fabric failure or tear could potentially cause the loss of the payload. Besides the expected aerothermal loading, a flexible TPS must be able to survive the mechanical loads exerted during packing, deployment and aerodynamic flow [1].

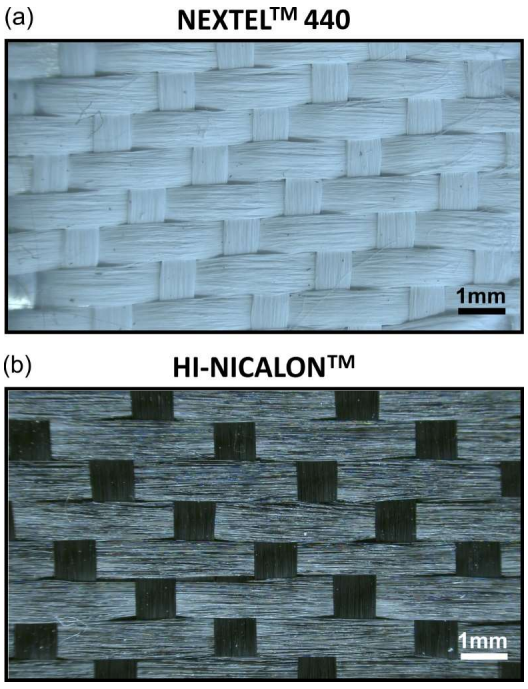

Figure 1.2: Optical image of a 5-harness satin fabric of (a) Nextel-440, (b) Hi-Nicalon

To predict the thermal response of a flexible TPS, multiple physical phenomena, such as pyrolysis or oxidation, must be considered. Proper modeling of solid conduction has proven to be a challenge because of gas conduction and radiative transport within the porous structure of the material [2]. Test gas infiltration within the materials porous structure during thermal evaluation of the flexible TPS has shown that gas type and superficial and interstitial pressure has a significant effect over the heat transfer of the material [2]. A 1D transient solution empirically fit model has been developed through COMSOL [4] to study the response and performance of different ground tested lay-up structures. Two main candidates for the high temperature woven ceramic fabrics are Nextel-BF20 and Hi-Nicalon (Figure 1.2). Tests over a lay-up of two layers of Nextel-BF20, two layers of Pyrogel 3350 and two layers of Kapton (Figure 1.3), and tests over an equivalent lay-up replacing Nextel-BF20 by Hi-Nicalon, show that Hi-Nicalon (Figure 1.4) survives a 100 W/cm2 incident flux at relevant pressures while Nextel-BF20 survives a 20 W/cm2 flux. A study by Owens et al. [5] using a 30kW ICP torch for material testing showed that above 80 W/cm2, Hi-Nicalon samples were destroyed. However, the lack of a 3D model without empirically fitted parameters, that accounts for the physics involved, prevents from generating accurate thermal analysis of different material lay-ups in relevant environments [3].

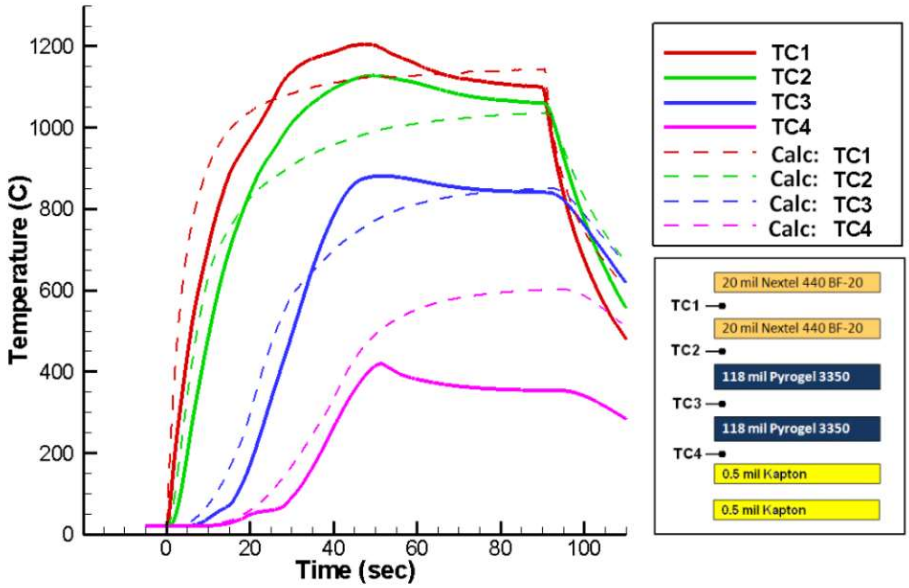

Figure 1.3: Laser-Hardened Materials Evaluation Laboratory thermocouple temperature measurements (solid) and calculated temperature results (dashed) at various layers for the baseline TPS test at a heat flux of 20 W/cm2 for 90 seconds. Reprinted from: Del Corso, Joseph A. et al 21st AIAA Aerodynamic Decelerator Systems Technology Conference and Seminar, Vol. 1, 2011, pp.139–161. In the public domain.

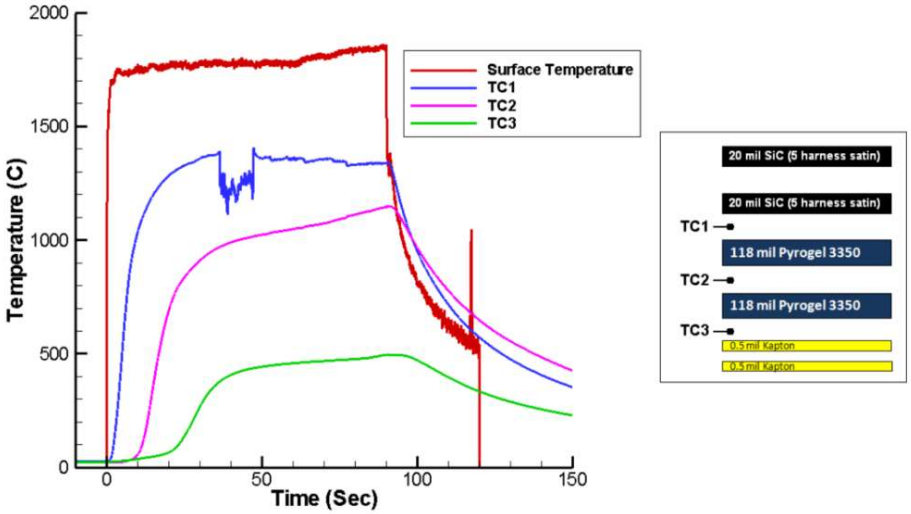

Figure 1.4: Laser-Hardened Materials Evaluation Laboratory thermocouple temperatures at various layers for the SiC 5HS layup tested at a heat flux of 100 W/cm2 and pressure of 8 torr for 90 seconds. Reprinted from: Del Corso, Joseph A. et al 21st AIAA Aerodynamic Decelerator Systems Technology Conference and Seminar, Vol. 1, 2011, pp.139–161. In the public domain.

1.2 High temperature woven ceramic fabrics

As commented above, two outer fabric materials are being evaluated, Nextel-BF20 that is considered a first-generation flexible thermal protection system (FTPS) material, and Hi-Nicalon, considered a second-generation FTPS.

Nextel-BF20

Nextel-BF20 (Figure 1.2 (a)) is the designation for Nextel-440 fibers woven in a 5-harness satin pattern and having a nominal count of fibers per yarn of 750. Nextel-440 fibers are an aluminoborosilicate type of fiber produced and commercialize by Minnesota Mining and Manufacturing Corporation (3M) and have a composition of 70 wt% Al2O3, 28 wt% SiO2, and 2 wt% B2O3. Nextel-440 fibers have a density of 3.05 g/cm3, an elastic modulus of 190 GPa, a tensile strength of 2GPa and a coefficient of thermal expansion of 5.3 ppm/K [6,7]. The microstructure of these fibers is characterized by a mullite phase and γ- Al2O3 crystallites in an amorphous silica matrix, the diameter of the fibers is 10-12 μm. Heat treatment at 1200 °C promotes a change into fine-grained (80 nm mean grain size) mullite, dropping the tensile strength to 1.6 GPa. Further heating leads to mullite grain coarsening (135 nm at 1400 °C) and considerable reduction of strength to 1.1 GPa (1400 °C) [8]. The continuous temperature use is set at 1370 °C [3]. Due to the lack of literature data on the thermal conductivity of Nextel-440, in this research, it is assumed that the thermal conductivity is that of mullite.

Hi-Nicalon

Hi-Nicalon (Figure 1.2 (b)) fibers, produced by Nippon Carbon Co. Ltd. and commercialized by COI Ceramics Inc. in the U.S., is a high temperature ceramic fiber formed by a β-SiC nanocrystalline (5-10 nm) structure and excess carbon in the grain boundaries with a composition of 62 wt% Si, 37 wt% C and 0.5 wt% O. Hi-Nicalon fibers have a nominal density of 2.74 g/cm3, an elastic modulus of 270 GPa and a tensile strength of 2.8GPa at room temperature [7,9].

Hi-Nicalon fibers are found to be creep resistant below 1000 °C, creep is observed at 1400 °C and is explained by grain boundary sliding. They keep linear elasticity up to 1350 °C. They form a passivating silica layer that aids oxidation resistance and restricts the diffusion of SiO and CO gases up to 1400 °C [7]. The maximum continuous use temperature for Hi-Nicalon fibers is 1800 °C [3]. Thermal conductivity at room temperature for Hi-Nicalon fibers have been reported as 8 W/m/K by Yamada et al. [10] and 7.7 W/m/K by Urano et al. [11].

1.3 Objectives

Altogether, given the flexible and porous nature of these ceramic fabrics and the high thermal and mechanical reliability they need to guarantee the integrity of the underlying structure, the design and performance study of these lay-up structures require a precise thermo-mechanical model. To aid the modeling efforts driven to achieve a fully capable physics-based model, this thesis focuses on:

- Development of a rapid conductivity testing methodology to measure thermal conductivity anisotropic behavior in 2D woven ceramic fabrics under mechanical loading with varying gas pressure conditions.

- Development of a thermo-mechanical model capable of accurately predicting the out-of-plane thermal conductivity of 2D woven ceramic fabrics under different mechanical loading conditions.

- Study of the confined gas thermal conductivity and its influence in the overall thermal behavior of the ceramic fabric material.

This thesis is organized as follows. Chapter 2 presents the development of an experimental methodology using the hot-disk transient plane source technique and a thermo-mechanical finite element model to study effects of deformation on anisotropic thermal conductivity of 2D woven ceramic fabrics. In Chapter 3 a multiscale model is created to predict the out-of-plane thermal conductivity at the micro- and meso-levels of transversely loaded 2D woven ceramic fabrics at different gas pressure conditions. The results are validated experimentally by applying the anisotropic hot-disk transient plane source method. A summary of the major conclusions and ideas for further development of this project are presented in Chapter 4.

References

[1] S.J. Hughes, J.S. Ware, J.A.D. Corso, R.A. Lugo, Deployable aeroshell flexible thermal protection system testing, 20th AIAA Aerodyn. Decelerator Syst. Technol. Conf. (2009) 1–21.

[2] M.A. Joseph A. Del Corso, Walter E. Bruce, III, Stephen J. Hughes, John A. Dec, Marc D. Rezin, and F.M.C. B. Meador, Haiquan Guo, Douglas G. Fletcher, Anthony M. Calomino, Flexible Thermal Protection System Development for Hypersonic Inflatable Aerodynamic Decelerators 9 Th International Planetary Probe Workshop, (2012).

[3] J. Del Corso, F. Cheatwood, W. Bruce, S. Hughes, A. Calomino, Advanced high-temperature flexible TPS for inflatable aerodynamic decelerators, 21st AIAA Aerodyn, Decelerator Syst. Technol. Conf. Semin. (2011) 1–23.

[4] COMSOL Multiphysics®. www.comsol.com. COMSOL AB, Stockholm, Sweden

[5] W. Owens, Aero-Thermal Characterization of Silicon Carbide Flexible Tps Using a 30Kw Icp Torch, University of Vermont, 2015.

[6] A.R. Bunsell, Oxide fibers for high-temperature reinforcement and insulation, Jom. 57 (2005) 48–51.

[7] D. Schawaller, B. Clauß, M.R. Buchmeiser, Ceramic filament fibers - A review, Macromol. Mater. Eng. 297 (2012) 502–522.

[8] T.O.F. Contents, Journal of the European Ceramic Society, J. Eur. Ceram. Soc. Artic. Press. (2013) 1–11

[9] T. Ishikawa, Recent developments of the SiC fiber Nicalon and its composites, including properties of the SiC fiber Hi-Nicalon for ultra-high temperature, Compos. Sci. Technol. 51 (1994) 135–144.

[10] R. Yamada, N. Igawa, T. Taguchi, S. Jitsukawa, Highly thermal conductive, sintered SiC fiber-reinforced 3D-SiC/SiC composites: experiments and finite-element analysis of the thermal diffusivity/conductivity, Journal of Nuclear Materials, 307–311 (2) (2002) 1215-1220.

[11] A Urano, A Saeki, M Takeda, A Yokoyama, Oxidative degradation behavior of polycarbosilane-derived silicon carbide fibers, Ceram. Eng. Sci. Proc., 20 (3) (1999) 85

CHAPTER 2: ANISOTROPIC THERMAL CONDUCTIVITY UNDER COMPRESSION IN TWO-DIMENSIONAL WOVEN CERAMIC FIBERS FOR FLEXIBLE THERMAL PROTECTION SYSTEMS

Abstract

Flexible thermal protection materials made from two-dimensional woven ceramics fibers are of significant interest for hypersonic inflatable aerodynamic decelerators being developed by NASA for future missions on Mars and other planets. A key component of the thermal shield is a heat-resistant outer ceramic fabric that must withstand harsh aero-thermal atmospheric entry conditions. However, a predictive understanding of heat conduction processes in complex woven-fiber ceramic materials under deformation is currently lacking. This article presents a combined experimental and computational study of thermal conductivity in 5-harness-satin woven Nextel 440 fibers, using the hot-disk transient plane source method and computational thermo-mechanical modeling by finite-element analysis. The objective is to quantify and understand the effect of compressive strain on anisotropic heat conduction in flexible two-dimensional ceramic materials. We find, both experimentally and theoretically, that thermal conductivity of woven fabrics rises in both in-plane and out-of-plane directions, as the transverse load increases. Air gap conduction and fiber-to-fiber contacts are shown to play a major role in this behavior. Our finite-element simulations suggest that the thermal conductivity anisotropy is strong because heat transfer of air confined between fibers is reduced compared to that of free air. The proposed modeling methodology accurately captures the experimental heat conduction results and should be applicable to more complex loading conditions and different woven fabric materials, relevant to extreme high temperature environments.

Nomenclature

440	Nextel fiber type
BF20	Nextel fabric type
FEA	finite element analysis
HIAD	hypersonic inflatable aerodynamic decelerator
RVE	representative volume element
SEM	scanning electron microscopy
TPS	thermal protection system
A	cross-sectional area of RVE
A_{FEA}	cross-sectional area of the yarn in the FEA model
A_{fiber}	cross-sectional area of a single fiber
A_{yarn}	total cross-sectional area of fibers in a yarn
Cp	specific heat capacity
D	dimensionless function
d	distance/gap between nodes
E	Young's modulus
E_{fiber}	Young's modulus of the fiber
G	shear modulus
h	distance between sensor and sample boundary
K	thermal conductivity
K_{fiber}	thermal conductivity of single fibers
K_{air}	thermal conductivity of air

$n_{fibers/yarn}$	nominal count of fibers per yarn
P_o	output power
Q	heat flow
R	hot-disk resistance
r	radius of the double spiral
T	temperature
t	time
V	volume fraction
V_{air}	volume fraction of air
V_{fiber}	volume fraction of fiber
V_{fiber}^{0}	initial volume fraction of fiber
X_i	cartesian direction of the RVE
x	dimension of the RVE

Greek Letters

α	temperature coefficient of resistance
Δ	difference operator
ϵ	strain
κ	thermal diffusivity
λ	gap thermal conductance
ν	Poisson's ratio
ρ	density

σ	stress
τ	dimensionless time

Subscripts

air	air property
eff	effective property
FEA	FEA model cross-section of the yarn
fiber	fiber property
yarn	yarn property
i	direction index
in	in-plane property
out	out-of-plane property

Superscripts

0	initial property
I, II, III	diagonal components of conductivity matrix for the fabric

2.1 Introduction

The expected increase in size and weight of future space missions constitutes an important technological challenge for current supersonic parachutes. An alternative technology developed by NASA is the Hypersonic Inflatable Aerodynamic Decelerator (HIAD). This deployable structure provides a larger drag area to afford higher Mach numbers and dynamic pressures than those currently possible with supersonic parachutes, making high-load deceleration at low ballistic coefficients possible. To protect the decelerator and payload from excessive heating during hypersonic atmospheric entry [1], the HIAD requires a flexible thermal protection system (TPS) consisting of a lay-up of flexible insulating materials, with an outer skin made of heat-resistant ablative insulators, typically high temperature woven ceramic fabrics. In the study of pyrolysis, oxidation and thermal performance of TPS materials, heat conduction through this outer fabric plays an essential role.

A woven fabric can be described as a hierarchically ordered multiscale material with 3 distinctive structural levels: fabric, yarn and fiber as shown in Figure 2.1(a)-(c), respectively. At microscopic scale, properties of the fibers together with their arrangement inside the yarn control the anisotropic behavior in yarns. At higher scale, the effective thermal properties and arrangement of the yarns influence the fabric properties [2]. Baxter et al. and Siddiqui et al. [3,4] studied different steady state methods to obtain thermal conductivity of fabrics from thermal resistance measurements. Other studies [5,6,7] have explored the use of static and dynamic methods to characterize the thermal conductivity of

non-woven and woven textiles. Maqsood et al. [8] measured the effect of compression and temperature on the thermal conductivity of non-woven ceramic fiber insulators using the transient plane source method. Zhao et al. [9] described the effect of pressure and temperature on the thermal conductivity of non-woven ceramic fiber insulators for TPS using a steady state apparatus. Abdel-Rehim et al. [10] studied the use of textiles as thermal insulators. Pradère et al. [11] determined that ceramic micro-fibers follow the thermal conductivity of bulk materials they are made of. Despite all past efforts, however, our means to locally quantify anisotropic heat transfer in two-dimensional (2D) woven fabric materials remains limited.

Physics-based modeling has been proposed to study the thermal behavior of flexible TPS under different environmental conditions [1]. Different computational methods for woven structures [12,13,14] have been created to model heat transfer [15] and mechanical deformation [16] in HIAD fabric materials. Lin et al. developed non-linear finite-element analysis (FEA) models to investigate textile deformation under different loading conditions [17,18]. Several modeling studies have focused extensively on the thermo-mechanical behavior of woven fiber-reinforced composites [19-23]. Siddiqui et al. [4] have proposed a model for the effective thermal conductivity through a dry fabric. However, no predictive model exists to study the anisotropic behavior of dry fabrics under combined mechanical and thermal loading.

Owens et al. [24] studied embrittlement mechanisms due to oxidation occurring in SiC fabric materials when exposed to harsh oxygen plasma environments. However, no computational model currently exists for simulating these mechanisms on the micro scale. To achieve this goal, it is necessary to develop models that can handle heat transfer property changes over complex woven structures and mechanical loadings.

The objective of this article is to understand and model the effects of deformation (compressive strain) on the anisotropic thermal conductivity of 2D woven ceramic fabrics at room temperature, by using the hot-disk transient plane source method and three-dimensional thermo-mechanical FEA modeling. The article is organized as follows. Section 2 describes the experimental methodology, including materials used, experimental procedure and a brief description of the theory behind the transient plane source method. The experimental results are presented in Section 3. Section 4 provides a description of the proposed FEA modeling, such as geometry modeling and implementation of mechanical compression and heat transfer simulation. The FEA simulation results are presented in section 5. Simulated and experimental results are compared and discussed in Section 6.

2.2 Materials and experimental methods

2.2.1 Materials

Woven alumina-based NEXTEL 440 micro fibers with a 5-harness satin pattern (NEXTEL BF20. 3M, St Paul, MN, USA) were used for this study. NEXTEL 440 fibers are aluminoborosilicate materials in consideration for HIAD applications [1]. The

composition is Al2O3 70%wt, SiO2 28%wt, B2O3 2%wt. The fibers have a filament diameter of 10-12 μm and the nominal filament count for a single yarn is 750 fibers. For handling purposes during the weave process, the fibers are coated with an organic material (sizing) that evaporates under relatively low temperatures [25]. No heat treatment was performed before thermal conductivity measurements. The fabric was cut in 40×40 mm2 samples, the thickness of the fabric samples was 0.55 mm. A rotary blade and a self-healing mat were used to minimize distortion on the weave pattern during the cutting process.

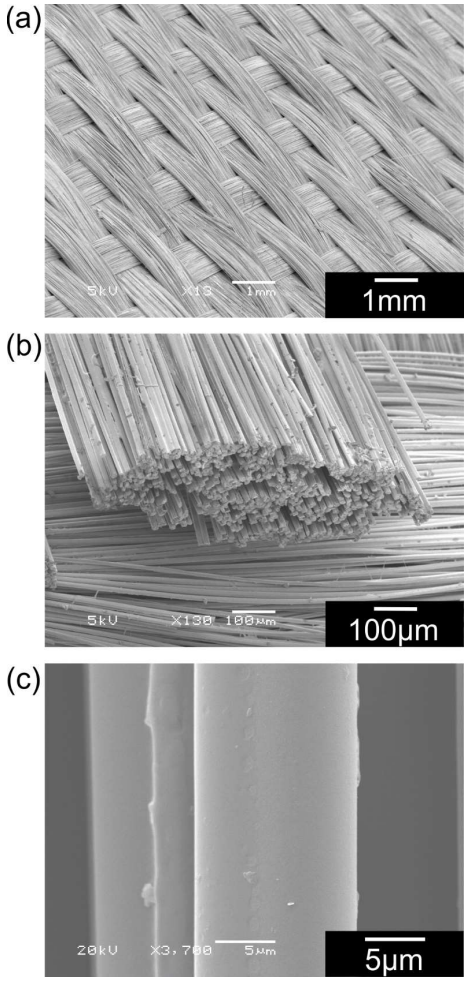

Figure 2.1: Alumina-based Nextel BF20 hierarchically ordered multiscale structure. Scanning electron microscopy images of (a) a woven fabric, (b) a yarn section, and (c) a single Nextel 440 fiber, inside the yarn.

2.2.2 Transient plane source theory

Thermal conductivity was measured by the transient plane source technique, which is based on the use of a planar element that acts as both heat source and temperature sensor [26,27]. Gustavsson et al. [28] and Michael et al. [29] have shown that this technique can simultaneously measure thermal conductivity on the in-plane and out-of-plane directions, allowing for anisotropic thermal property characterization. The sensor consisted of a 10 μm-thick nickel foil shaped as a double spiral (Figure 2.2(b)). The spiral was embedded between two 25 μm-thick films of Kapton serving as electrical insulators. A requirement to successfully implement the transient plane source method was to consider the sample, from the perspective of the sensor, to be infinite in all directions. In practice, this requirement imposed that the transient heating event could not reach sample boundaries during the temperature recording time. The distance travelled by the heat wave is a function of the sample thermal diffusivity and experimental time. In this study, the travel distance ranged from 0.6 to 0.8 mm in the out-of-plane direction, and from 4.25 to 4.60 mm in the in-plane direction. According to Michael et al. [29], the experimental time t must meet: $t \ll (h_{in}/2)^2/(\kappa_{in})$ and $t \ll h_{out}^2/(\kappa_{out})$, where h is the distance from the sensor to the sample boundary and κ is the thermal diffusivity, the in and out subscripts denote the in-plane and out-of-plane directions, respectively, as shown in Figure 2.2(a).

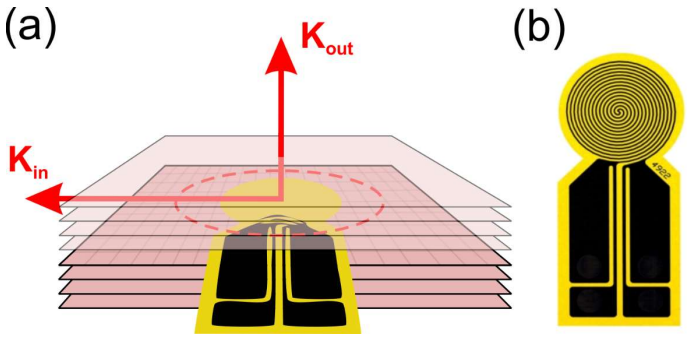

Figure 2.2: (a) Schematic of the transient plane source experiment. (b) Hot-disk sensor.

The plane element was placed between two material samples as schematically illustrated in Figure 2.2(a). A limitation of this method was to average the thermal conductivity through the distance travelled by the heat wave.

The sensor was designed to have a uniform power density. One pair of electrodes was used to supply heating power. The other pair measured the variation in temperature $\Delta T(t)$ through the change in resistance $R(t)$ using the following equation:

$$R(t) = R_0\big(1 + \alpha\Delta T(t)\big) \tag{2.1}$$

where R_0 is the initial resistance and α is the temperature coefficient of resistance. The solution of Fourier's law for heat conduction was applied to the geometry of the sensor by assuming an infinite transversely isotropic media and by spatially averaging the temperature over the area of the spiral as follows [26-29]:

$$\Delta\bar{T}(\tau_{in}) = \left(\frac{P_0}{\left(\pi^{\frac{3}{2}} r \sqrt{K_{in} K_{out}} \right)} \right) D(\tau_{in}) \tag{2.2}$$

where P_0 is the output power, r is the radius of the sensor, K_{in} and K_{out} are the in-plane and out-of-plane thermal conductivity of the media around the sensor, respectively (Figure 2.2(a)). $D(\tau_{in})$ is a dimensionless time function given in Ref. [29] and τ_{in} is defined as:

$$\tau_{in} = \frac{\sqrt{\kappa_{in}\, t}}{r} \tag{2.3}$$

Here, κ_{in} represents the thermal diffusivity of the sample in the in-plane direction and t the transient recording time. Theoretically, an ideal value for κ_{in} yields a linear relation between $\Delta\bar{T}(\tau_{in})$ and $D(\tau_{in})$. Numerically, this value was determined iteratively until linearity of Eq. (2.2) was approximately satisfied. The in-plane thermal conductivity (K_{in}) was then calculated as:

$$K_{in} = \left(\rho C_p\right)\kappa_{in} \tag{2.4}$$

where $\left(\rho C_p\right)$ is the volumetric specific heat capacity, which was obtained by transient plane source method as described by Gustavsson et al. [30]. Finally, thermal conductivity in the out-of-plane direction (K_{out}) was found by substituting Eq. 2.4 into Eq. 2.2 and equating to the slope of the line obtained numerically.

2.2.3 Experimental procedure

Data acquisition and post-processing were performed with a hot-disk TPS2200 analyzer (Thermtest, Fredericton, NB, Canada), which had an accuracy > 95% and repeatability > 99%. Hot-disk analyzers have been used in the past to study materials with similar composition and thermal properties, such as alumina/silica composites [31] and high porous mullite insulators [32]. The calculation of the volumetric heat capacity was performed using the heat capacity module of the TPS2200 analyzer. To meet the infinite media requirement, a stack of 4 fabric samples was used on each side of the sensor (Figure 2.3). Two different sensors of radius $r = 3.2$ mm and 6.4 mm, respectively, were used, but no difference was found in our measurements. Also, a minimum output power P_0 was required to obtain a smooth evolution between temperature increase and experimental time, noting that low powers generally produced noticeable noise on the temperature signal. Therefore, the optimum input parameters were determined iteratively with different recording times and powers to meet the above requirements. In this study, we used $P_0 = 35$ mW and a transient recording time of $t = 10$s.

To optimize the contact between sensor and specimen, we applied a transverse pressure using a screw as shown in Figures 2.3 (a) and (b). A load cell, with 100lb capacity and accuracy > 99.5% (iLoad mini, Loadstar Sensors, Fremont, CA, USA), was added to the stacked set-up to measure the compression load. It should be noted that compression effects could be important because conduction is the primary mechanism of heat transport in fabrics [4] and its woven structure makes it more compressible. The applied load may

affect fiber contact not only within yarns, but also between single fabric layers. Wait times of 30 minutes were used between measurements to ensure the sample achieved thermal equilibrium and mechanical relaxation after applying a new compression load. A set of three thermal conductivity measurements was conducted for each applied load. Room conditions remained constant at 23±1 ºC for every measurement.

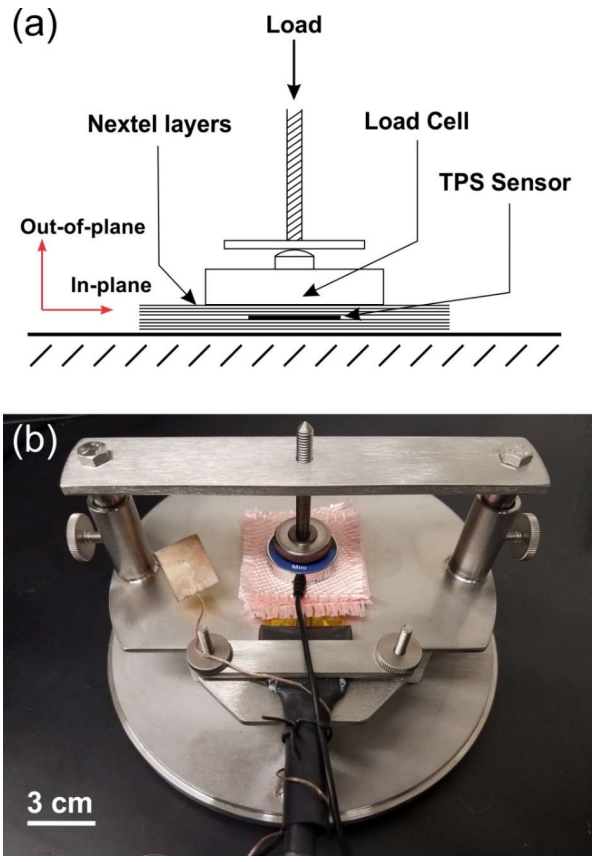

Figure 2.3: Experimental thermal conductivity characterization using the hot-disk transient plane source method. (a) Sketch of the set-up. (b) Optical image of the experimental sample holder.

2.3 Experimental results

Compression mechanisms in fabrics depend on fiber arrangement inside the yarn [12], which may lead to a load history dependency. To study this effect, 3 different loading patterns were tested, as shown in Figure 2.4(a). In Pattern 1, the pressure was increased monotonically between each measurement. In Pattern 2, the samples were first compressed, followed by a monotonic increase in load. In Pattern 3, the samples were completely un-loaded before the next increase in pressure, load and load-cell were removed and re-located between each measurement, to verify if conductivity was dependent on fiber rearrangement after re-loading.

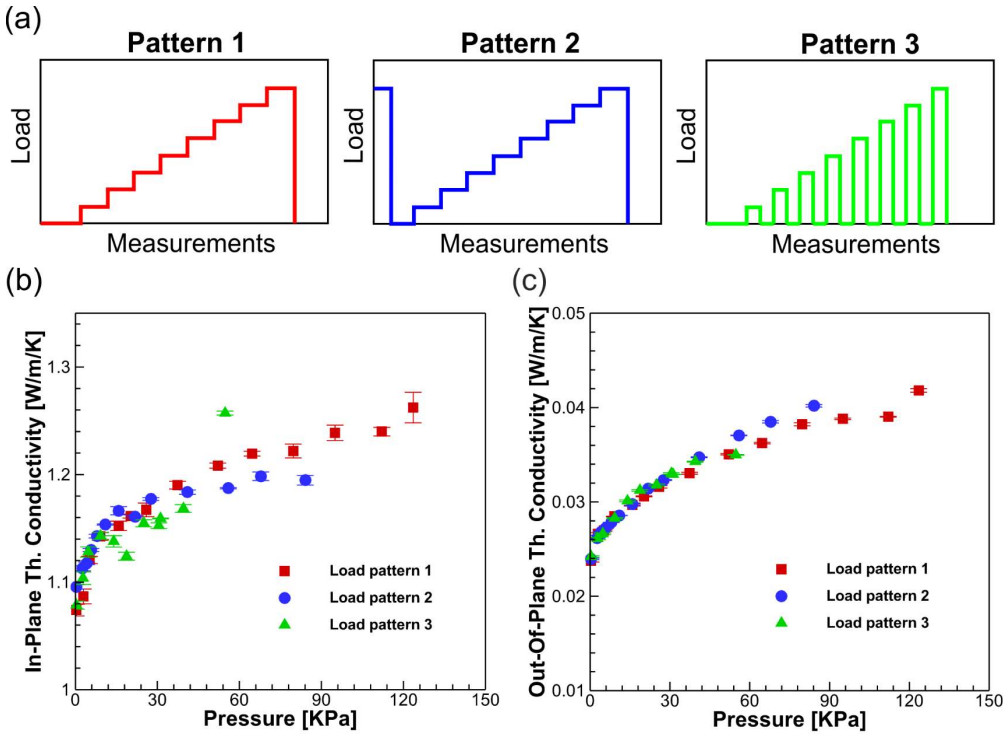

Figure 2.4: Experimental results. (a) Loading patterns studied. (b) In-plane and (c) out of plane thermal conductivity measurements in the fabric material subjected to the above loading patterns.

Figure 2.4(b) shows the evolution of the in-plane thermal conductivity measured as a function of the applied load, for the three loading patterns. We find that the thermal conductivity in the in-plane direction increases with applied load, with a steep increase in the first stage of compression, from 0 to 20 KPa. The standard deviation on our data was found less than 1%, except for the last data point of Pattern 1 for which it reached 2%. Loading Pattern 1 shows the smoothest increase in conductivity with applied pressure. Results from loading Pattern 2 follow those from Pattern 1 but starting at a higher conductivity, followed by a slower trend in the second stage of compression after 25 KPa. Results from loading Pattern 3 lead to more scattered conductivity data, but the overall trend remains the same as that for loading Patterns 1 and 2. The scattering is attributed to fiber rearrangement after each compression step. Nevertheless, the patterns show less than 6% difference at same applied pressure. Therefore, we can conclude that the loading pattern does not significantly influence our measurements.

Figure 2.4(c) presents the evolution of the out-of-plane thermal conductivity measured as a function of the applied load, for the three loading patterns. The out-of-plane thermal conductivity increases with applied pressure, as the in-plane thermal conductivity does. The thermal conductivity values for the out-of-plane direction are found to be two orders of magnitude smaller than those for the in-plane direction. The relative increase in conductivity is, however, steeper for the out-of-plane than the in-plane directions. The apparent measurement scattering observed for the in-plane thermal conductivity is not observed here, the relative increase in conductivity as compared to the in-plane

measurements may be masking this scattering. The three loading patterns result in the same change of conductivity with pressure. The standard deviation for each data point is observed to be small.

2.4 Computational finite element modeling

2.4.1 Geometry modeling

NEXTEL BF20 materials have a 5-harness satin weave. Due to its periodic structure, the fabric was modeled by its minimum representative volume element (RVE) or unit cell as shown in Figures 2.5 (a) and (b). The geometry of the RVE was identified by scanning electron microscopy (SEM). A computational model with periodic boundary conditions was generated using TEXGEN [15], an open source code for textile modeling, and exported to the FEA software ABAQUS [33]. The dimensions of the RVE prior to mechanical compression were $4.15 \times 5 \times 0.55$ mm^3. Each yarn was discretized using reduced integration 8-node and 6-node 3D elements with hourglass control. Because the fibers are arranged parallel to each other in the yarn, the longitudinal direction in each element was set locally to be tangent to the fiber path, and the transverse directions were oriented inside the cross-sectional plane as shown in Figure 2.5(d).

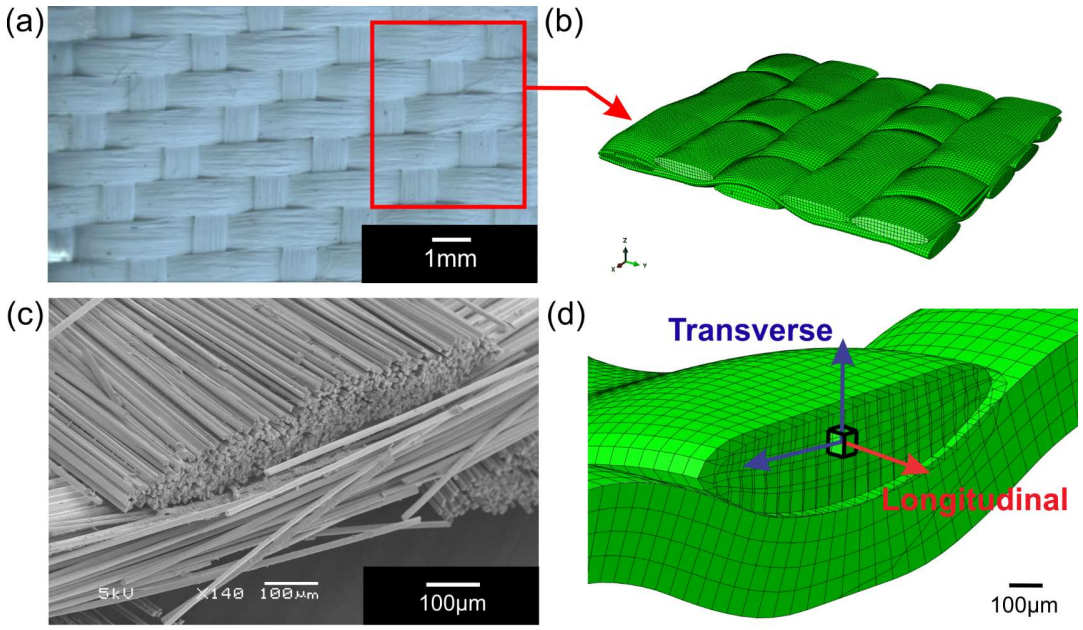

Figure 2.5: Representative volume element (RVE) modeling. (a) Optical image of Nextel BF20 woven fabric. (b) FEA model of the RVE. (c) SEM cross-sectional view of Nextel BF20 fabric. (d) FEA representation of the cross-sectional view and local coordinate system definition.

The volume fraction of fibers inside each yarn was calculated for every cross-section of yarn as follows:

$$V_{fiber}^{0} = \frac{A_{yarn}}{A_{FEA}} = \frac{n_{fibers/yarn} A_{fiber}}{A_{FEA}} \tag{2.5}$$

This description guarantees that the contribution of the fiber properties is consistent through the whole yarn even if the cross-sectional area varies. For simplicity, in this study, the distribution of fibers along the cross-section was kept uniform.

2.4.2 Mechanical simulation

The constitutive model for the mechanical behavior of the fabric under compression was implemented through a user material subroutine based on the work of Lin et al. [17]. The material constants were passed as properties (PROPS) to the user material subroutine in ABAQUS. The element volume fraction and initial transverse Young's modulus were passed as state variables (STATV). From the stiffness of an orthotropic material, we have:

$$\begin{Bmatrix} \epsilon_{11} \\ \epsilon_{22} \\ \epsilon_{33} \\ \epsilon_{23} \\ \epsilon_{13} \\ \epsilon_{12} \end{Bmatrix} = \begin{bmatrix} \frac{1}{E_{11}} & \frac{-\nu_{12}}{E_{11}} & \frac{-\nu_{13}}{E_{11}} & & & \\ \frac{-\nu_{12}}{E_{11}} & \frac{1}{E_{22}} & \frac{-\nu_{23}}{E_{22}} & & 0 & \\ \frac{-\nu_{13}}{E_{11}} & \frac{-\nu_{23}}{E_{22}} & \frac{1}{E_{33}} & & & \\ & & & \frac{1}{G_{23}} & 0 & 0 \\ & 0 & & 0 & \frac{1}{G_{13}} & 0 \\ & & & 0 & 0 & \frac{1}{G_{12}} \end{bmatrix} \begin{Bmatrix} \sigma_{11} \\ \sigma_{22} \\ \sigma_{33} \\ \sigma_{23} \\ \sigma_{13} \\ \sigma_{12} \end{Bmatrix} \tag{2.6}$$

where ϵ and σ are the strain and stress, respectively. ν, E and G are the Poisson's ratio, Young's modulus and shear modulus, respectively. Axis 1 was assigned to the longitudinal direction and axes 2 and 3 to the transverse directions of the local coordinate system.

Following Lin et al.'s study, for transversely isotropic yarn materials, we have,

$$E_{22} = E_{33} \tag{2.7}$$

$$\nu_{12} = \nu_{13} \tag{2.8}$$

$$G_{12} = G_{13} \tag{2.9}$$

The longitudinal modulus (E_{11}) of the yarn was approximated by the rule of mixtures. However, given that air does not contribute to the overall stiffness, the Young's modulus in the fiber direction was described as:

$$E_{11} = E_{fiber}V_{fiber} \tag{2.10}$$

The transverse modulus increases during compaction due to the reduction of air gaps [17]. Martin et al. [12] have shown that E_{22} can be obtained by:

$$E_{22}(\epsilon_{22}) = \frac{\sigma_{22}}{\epsilon_{22}} = \frac{-a\left(\frac{V_{fiber}^0}{\exp(\epsilon_{22})}\right)^b + a\left(V_{fiber}^0\right)^b}{\epsilon_{22}} \tag{2.11}$$

where a and b are experimental parameters obtained from fitting a power law to a yarn compression test. Parameters a and b depend on the initial configuration and arrangement of fibers prior to compaction, but also were taken as constant for simplicity. We used $a = 1151$ and $b = 12.24$ as suggested in Ref. [12].

The transverse shear behavior was calculated as:

$$G_{23} = \frac{E_{33}}{2(1+\nu_{23})} \tag{2.12}$$

The fabric compression was performed by adding two analytical rigid surfaces below and above the model. Mechanical contact between yarns, and yarn-to-plate contacts were considered as surface-to-surface interactions with a coefficient of friction of 0.3 and 0.5, respectively, as suggested in the literature [12]. Penalty contact was used to avoid element distortion.

A compressive strain of 30% was applied by imposing a uniform displacement to the top plate along the out-of-plane direction, while the bottom plate was kept fixed. The pressure applied over the fabric was calculated as the reaction force over the plates divided by the total area of the RVE.

2.4.3 Equilibrium heat transfer simulation

The equilibrium solution for thermal conductivity in the fabric was obtained by steady-state heat-transfer simulations over the RVE. The effective thermal conductivity tensor can be written as [34]:

$$K_{eff} = \begin{bmatrix} K_{eff}^{I} & 0 & 0 \\ 0 & K_{eff}^{II} & 0 \\ 0 & 0 & K_{eff}^{III} \end{bmatrix} \tag{2.13}$$

The model for this study assumed low temperatures and small gradients; therefore, radiation effects were considered negligible [4]. Also, we considered the air in steady-state condition and no heat transport through air convection, because gaps between fibers were small [4]. Therefore, thermal transport was exclusively treated as heat conduction.

The yarn is considered as a network of fibers with air gaps and contacts between fibers. Given the current lack of a yarn level-based model for dry fabrics (no solid matrix) and as suggested by Siddiqui et al. [4], a system with fiber and air connected in parallel was assumed for modeling thermal conductivity along the longitudinal direction:

$$K_{11} = K_{fiber}V_{fiber} + K_{air}\left(1 - V_{fiber}\right) \tag{2.14}$$

Similarly, a series model of fiber and air conductivities was used to approximate the transverse thermal conductivity of the yarn [4]:

$$K_{22} = \frac{K_{fiber}K_{air}}{K_{air}V_{fiber} + K_{fiber}\left(1 - V_{fiber}\right)} \tag{2.15}$$

By lack of literature data, thermal conductivity in a single fiber of Nextel 440, K_{fiber}, was estimated as follows. It has been observed that thermal conductivity in other types of Nextel fibers (e.g. Nextel 720) follows that of their bulk material counterpart [11]. Thermal conductivity of Nextel 440 (70% Al_2O_3, 28% SiO_2, 2% B_2O_3) was considered close to that of Mullite (approximately 71% - 72% Al_2O_3, + SiO_2) [35,36]. Figure 2.6 shows

that this estimate matches the conductivity of alumina with impurities obtained by extrapolating the values from the literature [37] to a 71% content of Al_2O_3. The final value was estimated as K_{fiber} = 7 W/m/K. Air conductivity at ambient temperature was taken as an initial value of K_{air} = 0.026 W/m/K [38].

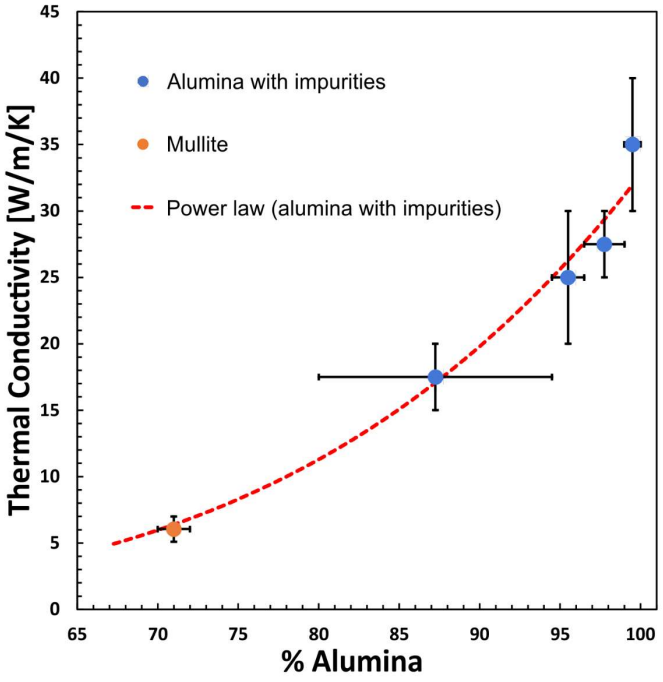

Figure 2.6: Thermal conductivity of some bulk aluminum oxide-based ceramics as function of alumina content.

To apply the thermal boundary conditions, air was first modeled as a meshed "fluid" matrix as suggested by Siddiqui and Sun [4]. However, the inability to perform a mechanical compression simulation over such a system led us to replace the air matrix through the gaps of the RVE in Figure 2.7(a), by a gap thermal conductance associated with a surface-to-surface thermal interaction between elements. As shown in Figure 2.7(b),

the gap thermal conductance λ was defined as a function of the distance between surfaces, *d,* such as [39]:

$$\lambda = \frac{K_{air}}{d} \tag{2.16}$$

Two thin plates with air thermal properties were created on top and bottom of the RVE to apply the boundary conditions, Figure 2.7(c). To test the validity of this second model with a new "dry" mesh, we run the same steady-state heat-transfer simulation in both systems (fluid mesh compared to air modelled as a gap conductance). Direct comparison between the two models could not be achieved during mechanical compression simulation, since air elements would instantaneously collapse under load. The difference on the thermal conductivity results between the two models was on the order of 10^{-4}, suggesting that the substitution of the air mesh by gap conductance boundary conditions was a suitable approximation.

The effective heat conduction through the unit cell was calculated by Fourier's law:

$$Q_i = -K_{eff}^{i} A_i \frac{\Delta T_i}{\Delta x_i} \tag{2.17}$$

where Q is the computed heat flow, K_{eff} is the effective thermal conductivity, A is the cross-sectional area of the RVE, Δx is the dimension of the unit cell, and ΔT is the temperature gradient. The index i represents cartesian directions (X_1, X_2, X_3) of the unit cell, as

represented in Figure 2.7(a). A steady-state heat-transfer simulation was performed in each direction (X_1, X_2, X_3), after each compression step. The thermal conductivities, K_{eff}^{i}, were calculated using Eq. 2.17 and the heat flow simulated from ABAQUS. Diffusive 8-node and 6-node 3D elements were used for these simulations.

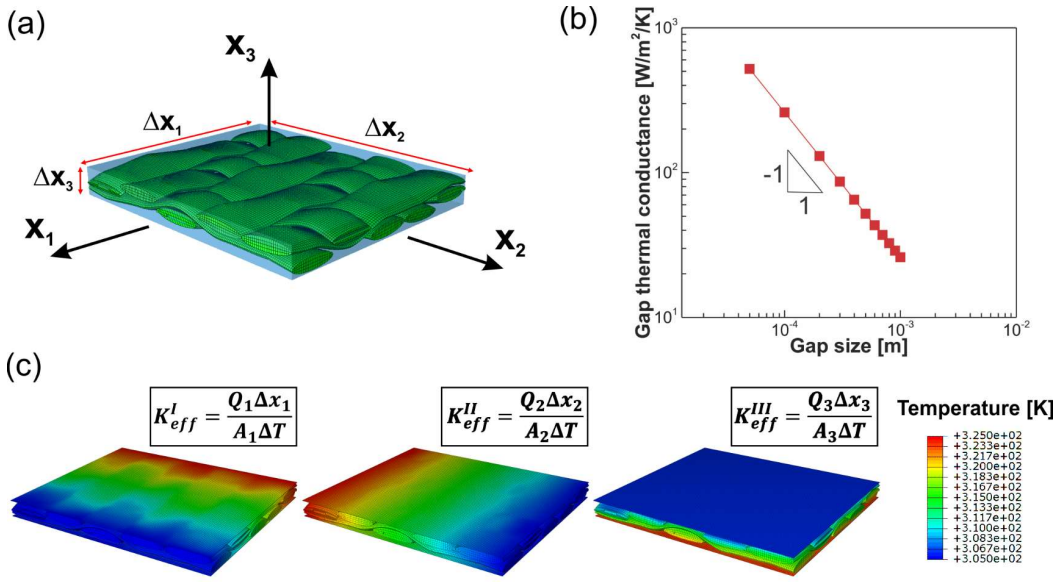

Figure 2.7: RVE boundary conditions for steady-state heat-transfer analysis. (a) RVE mesh surrounded by air. (b) Gap thermal conductance property. (c) Temperature profile of the RVE for the three temperature gradients applied as different boundary conditions.

2.5 Computational results

2.5.1 Simulated in-plane thermal conductivity results

As described above, the transient plane source method is limited to only in-plane and out-of-plane measurements. Due to this limitation, the simulated effective thermal

conductivities in the X_1 and X_2 directions were averaged into an effective "in-plane" thermal conductivity value. Figure 2.8 shows good agreement between the experimental results and the averaged in-plane conductivity from the FEA simulations. Qualitatively, the proposed FEA model captures the same behavior as that shown by the experiments, i.e. a steep non-linear rise of conductivity in the first stage of compression, followed by a softer linear increase above approximately 30 kPa. Quantitatively, the FEA solution becomes more accurate as compression increases, because the quantity of air inside the RVE is decreasing, which suggests that air conductivity requires a more complex model at small scale. Nevertheless, the difference between FEA solution and experiments in that region is less than 6%. Figure 2.8 shows that, by reducing K_{air}, the slope of the thermal conductivity variation with compressive strain decreases moderately.

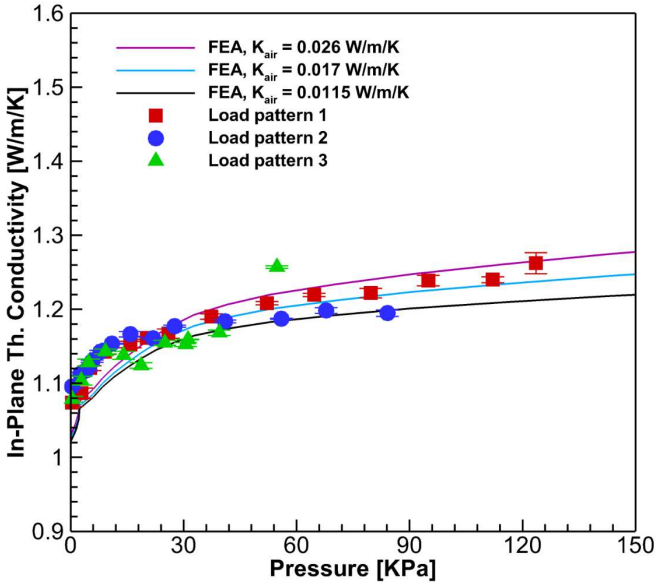

Figure 2.8: Simulated in-plane thermal conductivity for Nextel BF20 fabrics compared to the hot disk transient plane source measurements under compressive strain. K_{air} = 0.026 W/m/K represents the thermal conductivity of free air under normal steady state conditions.

2.5.2 Simulated out-of-plane thermal conductivity results

Figure 2.9 shows the comparison between the out-of-plane FEA results and the transient plane source measurements. We can observe that by using the initial value of K_{air}= 0.026 W/m/K, taken from free air at room conditions, the model overestimates the out-of-plane thermal conductivity of the fabric. Besides, from the experimental results, we observe that the thermal conductivity of the fabric before compression is already lower than this initial value. This indicates that the thermal behavior of free air may not be a valid assumption to model the thermal conductivity through the fabric. Due to the complexity of the geometry, air gaps and contacts, other contributions to the overall thermal conductivity may influence the effective value of K_{air}. As K_{air} is decreased, Figure 2.9 shows that the computed thermal conductivity better converges towards the experimental ones, matching the transient plane source measurements at a value of K_{air} = 0.0115 W/m/K.

Furthermore, a close-up view of the initial compression stages shows a sharp initial increase in thermal conductivity. This behavior is observed as well in the FEA solution and is attributed to the initial gap overclosure between yarns. Jump-to- contacts in the yarns reduce both the space between yarns and the overall amount of air inside the RVE, before internal strain is observed in the yarn.

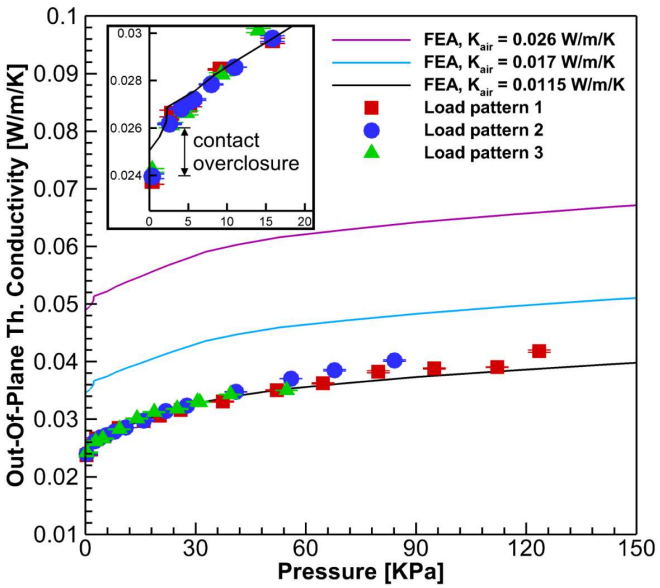

Figure 2.9: Simulated out-of-plane thermal conductivity for Nextel BF20 fabrics compared to the hot-disk transient plane source measurements under compressive strain. K_{air} = 0.026 W/m/K represents the thermal conductivity of free air. Contact overclosure is the jump to contact between freestanding fibers when loading is initiated.

2.5.3 Transverse E and K

Figure 2.10 shows the transverse Young's modulus (E_{22}) and transverse thermal conductivity (K_{22}) distribution over the RVE geometry at 30% compression. It can be seen that local thermal conductivities in transverse directions of the yarns have a similar behavior to the local transverse Young's moduli. The non-linear elasticity model used for modeling the mechanical behavior of the yarns (Eq. 2.11) dictates that stiffer elements are present where the local strain is larger. This effect is attributed to the packing density of the fibers that increases locally with strain.

The increase in local transverse stiffness observed in Figure 2.10(a) is, therefore, a consequence of the increasing local volume fractions during compression. These local volume fraction increments promote an increase in local conductivities on the transverse direction, as shown in Figure 2.10(c). Figure 2.10(b) represents the solution to Eq. 2.11 for the chosen values of a and b as a function of fiber volume fraction. This curve is in good qualitative agreement with that computed from per-element transverse thermal conductivity values as a function of the fiber volume fraction shown in Figure 2.10(d). Therefore, Figures 2.10 provides direct numerical evidence for a concurrent increase of both E and K, as the fiber volume fraction increases locally during compressive strain.

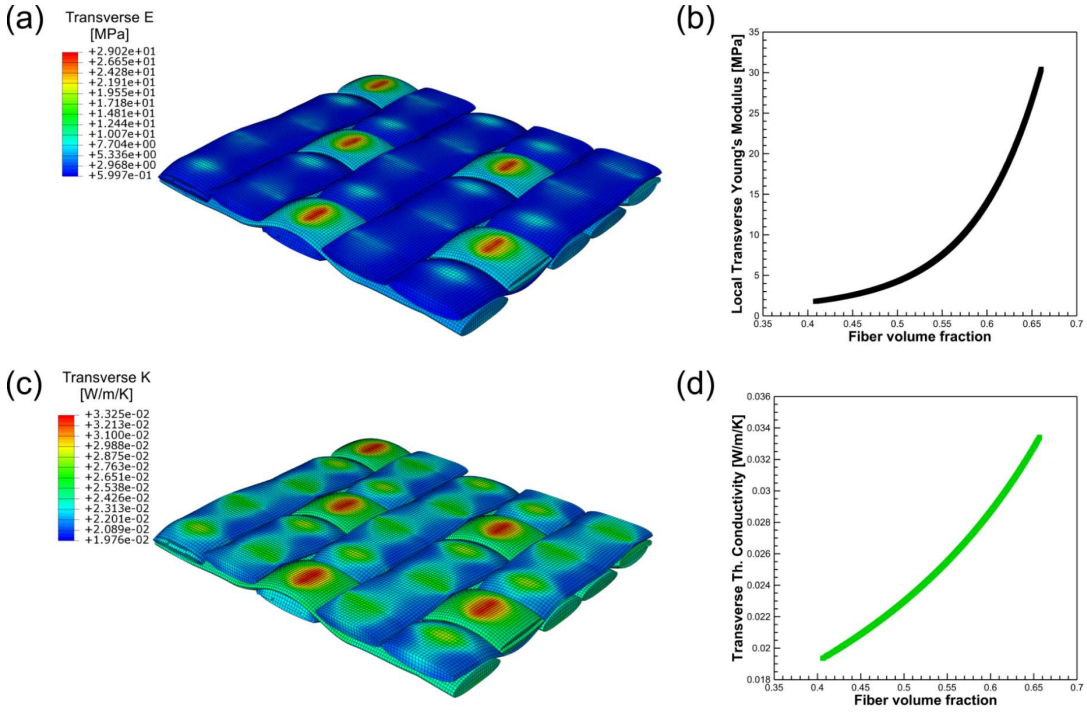

Figure 2.10: Microscale simulation results at 30% strain. (a) Transverse Young's modulus map. (b) Theoretical transverse Young's modulus as a function of local volume fraction of fibers. (c) Transverse thermal conductivity map. (d) Per-element local transverse thermal conductivity as a function of local volume fraction of fibers.

2.6 Discussion

2.6.1 Effects of compressive strain on thermal conductivity of 2D woven materials

Based on our experimental and FEA results in Figures 2.8 and 2.9, change in thermal conductivity with compression can be divided into three regimes. First, a steep and short increase in conductivity takes place at the very beginning of the curve up to 5 kPa. Our FEA simulations show that the fabric experiences a 5% compressive deformation during this stage; however, strain inside the yarns is not observed, suggesting that this effect is mainly produced by the initialization of contacts between yarns or overclosure effects. Second, the simulations predict that strain and contact area start to increase locally between yarns when loaded above 5 kPa, associated with a reduction of air gaps in the material. Therefore, thermal conductivity raises with applied pressure in both in-plane and out-of-plane directions. Third, the conductivity continues to progress more slowly at loads above 30 kPa, corresponding to a 17% total compression in the fabric material. At this stage, local strain through the yarns becomes increasingly significant, suggesting that the yarns have approached a jammed structure or locked state, and that the densification of fibers inside the yarns due to compression now predominantly influences heat transport.

2.6.2 Effects of thermal contact resistance and thermal conductivity of air

Figure 2.9 provides clear evidence that our FEA model and experiments are in good quantitative agreement only if K_{air} is decreased to 0.0115 W/m/K. This value is smaller than the commonly adopted value of K_{air} = 0.026 W/m/K for free air conduction. This

discrepancy appears to be more substantial for out-of-plane than in-plane directions. We can attribute these observations to several experimental and modeling factors as follows.

First, in the transient plane source analysis, a source of heat inside the material was assumed. Because this method is based on contact, however, it is possible that an extra resistance was formed on the contact between sensor and sample without being considered in the analysis. Another possibility could lie in the transient plane source method that does not account for transient effects on thermal conductivity of the air environment. Nevertheless, to mitigate these transient effects, we have imposed significant relaxation times between each measurement.

Second, regarding the modeling assumptions, we chose a reference thermal conductivity for air of 0.026 W/m/K for the whole model, which is the value of free air under normal steady-state condition at room temperature. However, it is possible that the air within the pores of the sample behaves differently due to spatial confinement. Lower thermal conductivity has been typically observed in micro and nano-spacing for aerogels and other insulators [9,40,41].

Third, another possible cause for this behavior could be related to the thermal contact resistance between fibers inside each yarn and that between the yarns [42-44]. Such resistances may have a pronounced influence on the series assumption used for determining the out-of-plane conductivity (Eq. 2.15). However, FEA modeling of every fiber contact

present inside a yarn would be computationally too prohibitive and was outside of the scope of the present study.

2.6.3 Thermal conductivity anisotropy in flexible 2D woven ceramic materials

Comparing the results in Figures 2.8 and 2.9 reveals a pronounced thermal conductivity anisotropy in the woven ceramic materials, which is defined in the following as the ratio of thermal conductivity between in-plane and out-of-plane directions, i.e. K_{in}/K_{out} or K_{11}/K_{22}. Figure 2.11 shows that the thermal conductivity anisotropy starts in the 40-45 range but surprisingly drops by 33% as the compression pressure increases to 120 kPa. This strain-dependent behavior primarily relates to the faster increase of K_{out} by 75%, compared to 17% for K_{in}, as shown in Figures 2.8 and 2.9, respectively. This phenomenon could be attributed to two strain-dependent effects at microscopic scale: A decrease in air volume fraction and an increase in fiber-to-fiber contact. On one hand, the overall reduction of air inside the RVE during compression drives the net increase of thermal conductivity in both in-plane and out-of-plane directions. However, Eqs. 2.14 and 2.15 indicate that the effect of air volume fraction affects both directions differently. On the other hand, heat on the in-plane direction is carried along the fibers and air, whereas in the out-of-plane direction, it must transfer across fibers through contacts and air. Furthermore, fiber-to-fiber contact effects should be expected to differ between the series and parallel models in our FEA simulations. Consequently, the increase of fiber-to-fiber contacts during compression could play a more important role on the out-of-plane thermal conductivity and the overall thermal transport anisotropy measured in woven fabric materials.

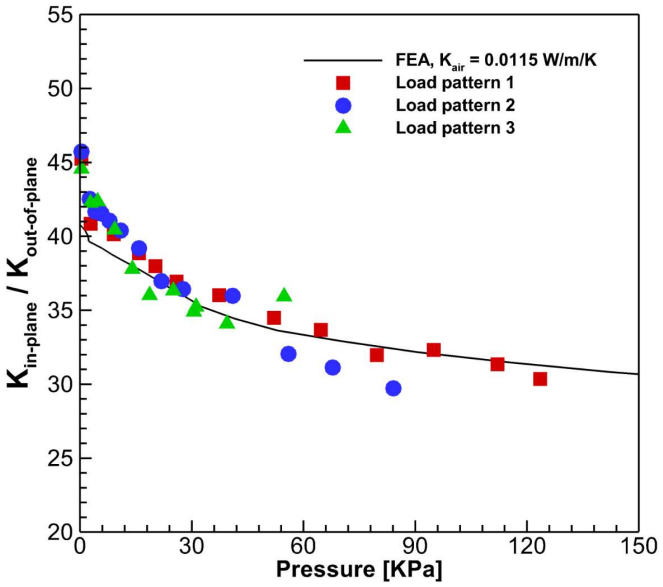

Figure 2.11: Comparison of simulated thermal conductivity anisotropy ratio to the hot- disk transient plane source measurements as a function of compressive pressure.

2.7 Conclusions

An experimental methodology was developed to measure and quantify the anisotropy of thermal conductivities in in-plane and out-of-plane directions of 2D woven ceramic fabric materials. A thermo-mechanical FEA model was created to simulate and study the evolution of this anisotropy under compressive strain in a Nextel BF20 woven fabric RVE, with constitutive equations integrating the volume fraction and orientation of fibers. The following conclusions can be drawn from the present study:

- Thermal conductivity in 2D woven fabric materials increases under out-of-plane compression, primarily due to the closure of gaps between yarns during the initial stages of compression, and densification of fibers in each yarn after fiber-to-fiber

contacts have been made. In parallel, thermal conductivity anisotropy between in-plane and out-of-plane directions decreases as pressure is applied.

- The model provided insights into the microscopic thermal behavior inside yarns, which could not be measured directly through the transient plane source method. We found a local relationship between thermal conductivity and elastic modulus throughout the fabric geometry, which is attributed to local variations in fiber volume fraction due to compression.

- FEA solution and transient plane source measurements showed excellent agreement when the conductivity K_{air} was decreased from 0.026 W/m/K (free air at room temperature) to 0.0115 W/m/K. The parametric study performed suggested that fiber-to-fiber contacts and air conduction in micro-spacing play essential roles on local heat transfer through the fabric.

This study shows that by applying the proposed methodology, the anisotropic thermal conductivity of a woven ceramic fabric can be effectively obtained if an accurate description of its geometry and single-fiber properties is available. Therefore, this method could be easily adapted to different woven materials of interest for high-temperature TPS applications, and to various loading conditions such as shear, tension or more complex loading problems.

References

[1] J. Del Corso, F. Cheatwood, W. Bruce, S. Hughes, A. Calomino, Advanced High-Temperature Flexible TPS for Inflatable Aerodynamic Decelerators, 21st AIAA Aerodyn. Decelerator Syst. Technol. Conf. Semin. (2011) 1–23.

[2] H. Bogaty, N.R.S. Hollies, M. Harris, Some Thermal Properties of Fabrics: Part I: The Effect of Fiber Arrangement, Text. Res. J. 27 (6) (1957) 445–449.

[3] S. Baxter, The thermal conductivity of textiles, Proc. Phys. Soc. 58 (1) (1946) 105–118.

[4] M.O.R. Siddiqui, D. Sun, Finite element analysis of thermal conductivity and thermal resistance behaviour of woven fabric, Comput. Mater. Sci. 75 (2013) 45–51.

[5] J.R. Martin, L. College, G.E.R. Lamb, Measurement of Thermal Conductivity of Nonwovens Using a Dynamic Method, Text. Res. J. 57 (12) (1987) 721–727.

[6] O. Jirsak, T. Gok, B. Ozipek, N. Pan, Comparing Dynamic and Static Methods for Measuring Thermal Conductive Properties of Textiles, Text. Res. J. 68 (1) (1998) 47–56.

[7] M. Mohammadi, P. Banks-Lee, P. Ghadimi, Determining Effective Thermal Conductivity of Multilayered Nonwoven Fabrics, Text. Res. J. 73 (9) (2003) 802–808.

[8] A. Maqsood, M. Anis-Ur-Rehman, V. Gumen, Anwar-Ul-Haq, Thermal conductivity of ceramic fibres as a function of temperature and press load, J. Phys. D. Appl. Phys. 33 (16) (2000) 2057–2063.

[9] S. Yuan Zhao, B. Ming Zhang, X. Dong He, Temperature and pressure dependent effective thermal conductivity of fibrous insulation, Int. J. Therm. Sci. 48 (2) (2009) 440–448.

[10] Z.S. Abdel-Rehim, M.M. Saad, M. El-Shakankery, I. Hanafy, Textile fabrics as thermal insulators, Autex Res. J. 6 (3) (2006) 148–161.

[11] C. Pradère, J.M. Goyhénèche, J.C. Batsale, S. Dilhaire, R. Pailler, Thermal diffusivity measurements on a single fiber with microscale diameter at very high temperature, Int. J. Therm. Sci. 45 (5) (2006) 443–451.

[12] S. Martin, Geometric and Mechanical Modelling of Textiles. PhD thesis, University of Nottingham, Nottingham, UK (2007).

[13] H. Lin, L.P. Brown, A.C. Long, Modelling and Simulating Textile Structures Using TexGen, Adv. Mater. Res. 331 (2011) 44–47. http://texgen.sourceforge.net

[14] WiseTex, S.V. Lomov, I. Verpoest, E. Bernal, F. Boust, V. Carvelli, J. Delerue, … F. Tümer, Virtual Textile Composites Software WiseTex: Integration with Micro-mechanical, Permeability and Structural Analyses." Fifteenth International Conference on Composite Materials 65 (15-16) (2005) 2563-2574. https://www.mtm.kuleuven.be/Onderzoek/Composites/software/ wisetex

[15] M. Ismail, A.S. Ammar, M. El-Okeily, 4. Heat transfer through textile fabrics: mathematical model, Appl. Math. Model. 12 (4) (1988) 434–440.

[16] J.L. Hill, R.D. Braun, Modeling of Plain Woven Fabrics for Inflatable Aerodynamic Decelerators, 55th AIAA/ASME/ASCE/AHS/ASC Structures, Structural Dynamics, and Materials Conference (2014) 1–12.

[17] H. Lin, M. Sherburn, J. Crookston, A.C. Long, M.J. Clifford, I.A. Jones, Finite element modelling of fabric compression, Model. Simul. Mater. Sci. Eng. 16 (3) (2008).

[18] H. Lin, M.J. Clifford, A.C. Long, M. Sherburn, Finite element modelling of fabric shear, Model. Simul. Mater. Sci. Eng. 17 (1) (2009).

[19] A. Dasgupta, R.K. Agarwal, S.M. Bhandarkar, Three-dimensional modeling of woven-fabric composites for effective thermo-mechanical and thermal properties, Compos. Sci. Technol. 56 (3) (1996) 209–223.

[20] H. Li, S. Li, Y. Wang, Prediction of effective thermal conductivities of woven fabric composites using unit cells at multiple length scales, J. Mater. Res. 26 (3) (2011) 384–394.

[21] A. Dixit, H.S. Mali, R.K. Misra, Unit cell model of woven fabric textile composite for multiscale analysis, Procedia Eng., Elsevier B.V. 68 (2013) 352–358.

[22] Q. Ning, T. Chou, A general analytical model for predicting the transverse effective thermal conductivities of woven fabric composites, Construction. (97) (1998) 315–322.

[23] Q.-G. Ning, T.-W. Chou, Closed-form solutions of the in-plane effective thermal conductivities of woven-fabric composites, Compos. Sci. Technol. 55 (1) (1995) 41–48.

[24] W. Owens, D. Merkel, F. Sansoz, D. Fletcher, Fracture Behavior of Woven Silicon Carbide Fibers Exposed to High-Temperature Nitrogen and Oxygen Plasmas, J. Am. Ceram. Soc. 98 (2015) 4003–4009.

[25] W. D. Bascom and S. Wong, The friction and wear of TPS fibers, Progress report on NASA grant NAG 2-444. (1987)

[26] Y. He, Rapid thermal conductivity measurement with a hot disk sensor: Part 1. Theoretical considerations, Thermochim. Acta. 436 (1) (2005) 122–129.

[27] S.E. Gustafsson, Transient plane source techniques for thermal conductivity and thermal diffusivity measurements of solid materials, Rev. Sci. Instrum. 62 (1991) 797–804.

[28] M. Gustavsson, H. Nagai, T. Okutani, Characterization of anisotropic and irregularly-shaped materials by high-sensitive thermal conductivity measurements, Solid State Phenomena 124-126 (2007) 1641-1644.

[29] N.K. Michael G. Miller, Jason M. Keith, Julia A. King, Brian J. Edwards, Measuring Thermal Conductivities of Anisotropic Synthetic Graphite–Liquid Crystal Polymer Composites, Polymer composites 27 (4) (2006): 388-394.

[30] M. Gustavsson, Specific heat measurements with the hot disk thermal constants analyser. Thermal Conductivity 23 (1996) 56-65.

[31] X. Wu, G. Shao, X. Shen, S. Cui, L. Wang, Novel Al_2O_3–SiO_2 composite aerogels with high specific surface area at elevated temperatures with different alumina/silica molar ratios prepared by a non-alkoxide sol–gel method, RSC Advances, 6 (2016) 5611-5620.

[32] M. Fukushima, Y. Yoshizawa, Journal of the European Ceramic Society Fabrication and morphology control of highly porous mullite thermal insulators prepared by gelation freezing route, J. Eur. Ceram. Soc. 36 (2016) 2947–2953.

[33] ABAQUS 2018, 2017, Dassault Systèmes Simulia Corp., Johnston, RI, USA.

[34] M. Villière, D. Lecointe, V. Sobotka, N. Boyard, D. Delaunay, Experimental determination and modeling of thermal conductivity tensor of carbon/epoxy composite, Compos. Part A Appl. Sci. Manuf. 46 (1) (2013) 60–68.

[35] L. Gong, Y. Wang, X. Cheng, R. Zhang, H. Zhang, Porous mullite ceramics with low thermal conductivity prepared by foaming and starch consolidation, J. Porous Mater. 21 (1) (2014) 15–21.

[36] D.J. Duval, S.H. Risbud, J.F. Shackelford, Mullite, (2008).

[37] P. Auerkari, Mechanical and physical properties of engineering alumina ceramics, Technical Research Centre of Finland, VTT Manufacturing Technology, Research Notes 1792 (1996) 3-36.

[38] R.B. Montgomery, Viscosity and Thermal Conductivity of Air and Diffusivity of Water Vapor in Air, J. Meteor. 4 (1947) 193-196

[39] A. Bejan, Heat Transfer Handbook, Wiley-Interscience, (3003)

[40] J.J. Zhao, Y.Y. Duan, X.D. Wang, B.X. Wang, Effects of solid-gas coupling and pore and particle microstructures on the effective gaseous thermal conductivity in aerogels, J. Nanoparticle Res. 14 (8) (2012) 1024.

[41] K. Daryabeigi, Thermal Analysis and Design of Multi-layer Insulation for Re-entry Aerodynamic Heating, 35th AIAA Thermophysics Conference 11-14 June 2001 Anaheim, Aerospace. (2001) 1-8.

[42] R. Arambakam, H. Vahedi Tafreshi, B. Pourdeyhimi, A simple simulation method for designing fibrous insulation materials, Mater. Des. 44 (2013) 99–106.

[43] R. Arambakam, H. Vahedi Tafreshi, B. Pourdeyhimi, Modeling performance of multi-component fibrous insulations against conductive and radiative heat transfer, Int. J. Heat Mass Transf. 71 (2014) 341–348.

[44] M. Bahrami, M.M. Yovanovich, J.R. Culham, Effective thermal conductivity of rough spherical packed beds, Int. J. Heat Mass Transf. 49 (2006) 3691–3701.

CHAPTER 3: MICROSCALE KNUDSEN EFFECT OVER THE OUT-OF-PLANE THERMAL CONDUCTIVITY OF WOVEN CERAMIC FABRICS UNDER COMPRESSION

Abstract

Flexible woven ceramic materials have shown remarkable results in the design of insulative lay-up structures for flexible thermal protection systems. A deeper understanding of thermal behavior through the different insulation layers is key for predicting the performance of the heat-shield layered structure. In this chapter, a thermo-mechanical multiscale model is developed to predict the out-of-plane thermal conductivity behavior at the micro- and meso-levels of transversely loaded two-dimensional woven ceramic fabrics. Knudsen effects within the multiscale structure are studied by adjusting gas pressure conditions. Alumina-based Nextel-BF20 and silicon carbide Hi-Nicalon with a 5-harness satin weave pattern are modeled by finite-element analysis. The computational results are validated experimentally by applying the anisotropic transient plane source method. We find that out-of-plane thermal conductivity drops with gas pressure due to Knudsen effects in the confined air within the fibrous structure. Volume fraction dependency of thermal conductivity contracts with pressure reduction. The multiscale approach yields a notable accuracy, with respect to simplified models, when compared with our experimental measurements. The proposed modeling technique is applicable to other fabric materials and loading conditions and presents an opportunity to study how changes within the fiber affect the overall thermal behavior.

Nomenclature

440	Nextel fiber type
5HS	5-harness satin weave type
BF20	Nextel fabric type
DEM	discrete element method
FEA	finite element analysis
HIAD	hypersonic inflatable aerodynamic decelerator
RVE	representative volume element
SEM	scanning electron microscopy
TPS	transient plane source
A	cross-sectional area of the RVE
Cond	gap thermal conductance
C_p	specific heat capacity at constant pressure
C_v	specific heat capacity at constant volume
D	dimensionless function
D_f	diameter of the fiber
d_1	characteristic length of a pore in the vertex region
d_2	characteristic length of a gap within fibers in the edge region
d_g	diameter of the gas molecule
K_{air}	thermal conductivity of air
K_{air0}	thermal conductivity of air in STP conditions
K_{fiber}	thermal conductivity of a fiber

K_B	Boltzmann's constant
K_{eff}	effective thermal conductivity of the model
Kn	Knudsen number
K_{in}	effective thermal conductivity in the in-plane
K_{out}	effective thermal conductivity in the out-of-plane
L	dimension of the microscale model
L_C	characteristic length
P	gas pressure
P_0	output power
Pr	Prandtl number
Q	Heat flow
r	radius of the sensor
T	temperature
V	volume fraction
V_{fiber}	volume fraction of fiber
x	distance travelled by the heat

Greek letters

α	accommodation coefficient
γ	adiabatic coefficient
Δ	difference operator
λ	molecular mean free path

ρ	density
τ	dimensionless time

Subscripts

0	initial condition
air	air property
eff	effective property
f	fiber property
g	gas property
in	in-plane property
out	out-of-plane property
p	constant pressure
v	constant volume

3.1 Introduction

In Chapter 2, a methodology to measure and quantify the anisotropic thermal conductivity of two-dimensional woven ceramic fabric materials was presented. To study this problem, a thermo-mechanical finite element model of the fabric was created. The model provided useful insights into heat conduction at the mesoscale in fabric materials under a transversal compressive load. A parametric study showed that to capture the correct behavior of the fabric in the out-of-plane direction, a more detailed description of the thermal behavior of confined air is necessary [1]. The precise modeling of the out-of-plane thermal conductivity is crucial for the design and analysis of the lay-up structure that integrates the HIAD's flexible thermal protection system [2].

As discussed in Chapter 2, from heat transfer perspective, a woven fabric is defined as a multiscale composite material with a porous structure consisting of a fiber reinforcement and a gaseous matrix ordered in 3 distinctive levels: fabric, yarn and fiber as shown in Figure 3.1. At microscopic scale, the properties of the fibers and confined gas together with their arrangement in the yarn control the thermal behavior of the yarn. Analogously, the arrangement and effective thermal properties of the yarns and gas determines the fabric properties at the mesoscale.

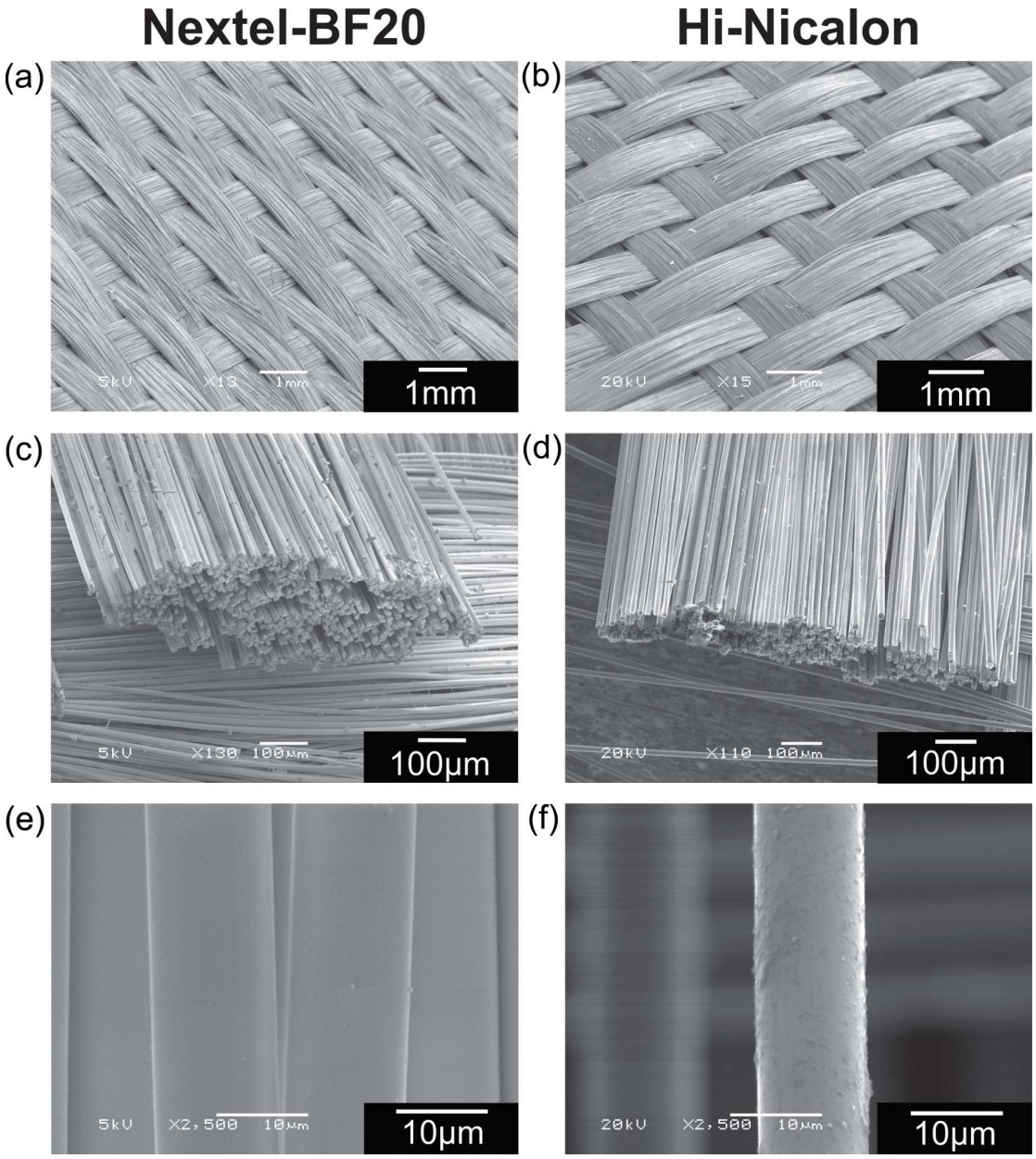

Figure 3.1: Alumina-based Nextel-BF20 and SiC Hi-Nicalon woven fabrics. Scanning electron microscopy images of (a)-(b) as received woven fabrics, (c)-(d) yarn sections, and (e)-(f) single fibers for heat-cleaned Nextel-440 and Hi-Nicalon, respectively.

Kaganer [3] described how the thermal conductivity of a gas is affected by being confined within a space with a characteristic length close or smaller to that of its molecular

mean free path. Multiple researchers have used this description to model gas conduction in porous materials, such as spherical beds or aerogels [4-7]. Other researchers [8, 9] have used one-dimensional differential equation formulations to describe the thermal conductivity and transient behavior of lay-ups of fibrous insulators while accounting for confined gas effects. Daryabeigi et al. [10, 11] studied the effect of pressure and temperature on the heat transfer of non-woven insulators for thermal protection systems, the gas behavior was modeled as a standard gas conduction model, using Kaganer's correction with an empirical fit for the characteristic length of the pore. Zhao et al. [12] applied the same methodology to treat the gas behavior in different fibrous materials. Lurie et al. [13] studied the influence of mean distance between fibers in the effective gas conductivity for non-woven materials. Despite all efforts, it is a general practice to treat thermal conductivity through fibrous insulators as a mixed series-parallel model or to use a semi-empirical formulation or an analytical solution of a simplified problem. However, a thermo-mechanical physics-based multiscale model that accurately captures the gas behavior at both micro- and meso-levels is still lacking to simulate the effective out-of-plane behavior of heat conduction through woven insulators.

The objective of this study is to model the out-of-plane thermal conductivity across the multiscale structure of woven fabrics and understand the effects of mechanical strain and gas pressure, by using the hot-disk transient plane source experiments with variable pressure, and multiscale three-dimensional thermo-mechanical FEA modeling. This chapter is organized as follows. Section 3.2. describes the experimental methodology and

materials. Section 3.3. provides a description of the proposed multiscale FEA model, such as the dynamics modeling and the heat transfer simulations for the micro- and meso-level models. The results from the computational models and the hot-disk measurements are presented and compared in Section 3.4. The effects of gas pressure and micro-spacing in woven fabric materials, advantages and limitations of the proposed multiscale model, and a comparison between the studied materials are discussed in Section 3.5.

3.2 Materials and experimental methods

3.2.1 Materials

Alumina-based Nextel-BF20 (3M, St Paul, MN, USA) and silicon carbide Hi-Nicalon (COI ceramics Inc., San Diego, CA, USA) woven fabrics with a 5-harness satin pattern were used for this study. The fabrics were cut in 40 x 40 mm^2 samples using a rotary blade and a self-healing mat to minimize distortion.

The fiber of Nextel-BF20 fabrics, Nextel-440, is an aluminoborosilicate material with a composition of Al2O3 70%wt, SiO2 28%wt, B2O3 2%wt [14]. The fibers had a filament diameter of 10–12 μm and the nominal filament count for a single yarn was 750 fibers. Prior to testing, the organic sizing of the Nextel fabric was removed by heat cleaning following the protocol suggested by the manufacturer. The samples were place into a furnace at room temperature, the temperature was ramped up to 700°C for 45 minutes and then kept at the prescribed temperature for 1 hour. The samples were left to cool to room temperature inside the oven. The sizing was removed to reduce off-gassing during vacuum

operations [15]. Due to the lack of literature data on the thermal conductivity of Nextel 440 fibers, it was approximated to that of mullite, 7 W/m/K [16]. The density was equal to 3.05 ± 0.03 g/cm^3, measured with a pycnometer and a high-precision scale.

Hi-Nicalon fibers consisted of a β-SiC nanocrystalline structure with a composition of Si 62%wt, C 37%wt and O 0.5%wt [17]. The fibers had a filament diameter of 14 μm and a nominal filament count of 500 fibers per yarn. A thermal conductivity of 8 W/m/K [18] was used for the Hi-Nicalon fibers. A density of 2.68 ± 0.03 g/cm3 was found by applying the same methodology.

3.2.2 Experimental procedure

Thermal conductivity was measured by the hot-disk transient plane source method. This technique is based on the use of a plane element that acts both as temperature sensor and heat source [19-22]. As discussed in the previous chapter (Section 2.2.2.), the solution of Fourier's law for heat conduction applied to this system was:

$$\Delta\bar{T}(\tau_{in}) = \left(\frac{P_0}{\left(\pi^{\frac{3}{2}} r \sqrt{K_{in} K_{out}} \right)} \right) D(\tau_{in}) \tag{3.1}$$

After postprocessing of the transient temperature-time data, the anisotropic experiment yields the product $K_{in}K_{out}$ and the thermal diffusivity $\kappa_{in} = K_{in}/(\rho C_p)$.

Finally, the volumetric heat capacity (ρC_p) is used to de-couple the conductivity values (Section 2.2.2).

A TPS2200 analyzer (Thermtest, Fredericton, NB, Canada), which had an accuracy >95% and repeatability >99% was used for data acquisition and postprocessing. The methodology to test anisotropic thermal conductivity of woven fabrics by using the hot-disk transient plane source method was developed in previous research [1] and is discussed in Section 2.2.3.

The volumetric heat capacity (ρC_p) was measured using the heat capacity module of the TPS2200 analyzer. However, the heat capacity measured using this method corresponds to that of a solid material without pores. Values of 2.3317 ± 0.0031 MJ/m^3/K and 1.8126 ± 0.0028 MJ/m^3/K were found for Nextel-440 and Hi-Nicalon, respectively. Similar values have been reported for fibers with a composition and structure close to the one of Hi-Nicalon [23]. By describing the fabric to be a composite with a gaseous matrix, however, a rule of mixtures was applied to account for the air contribution, such as

$$(\rho C_p)_{fabric} = V_{fiber}(\rho C_p)_{fiber} + (1 - V_{fiber})(\rho C_p)_{air} \tag{3.2}$$

where V_{fiber} is the volume fraction of ceramic fibers.

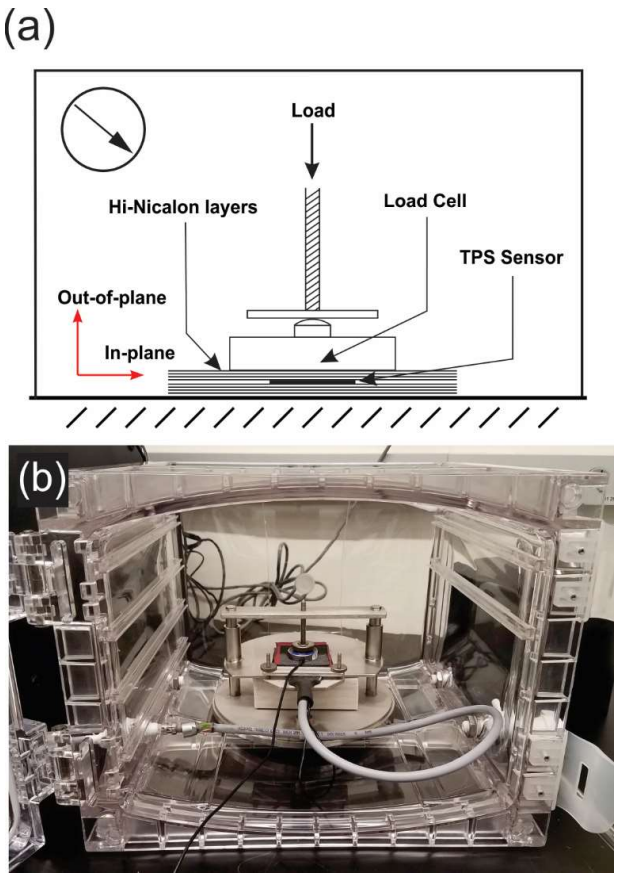

Figure 3.2: Experimental thermal conductivity characterization using the hot-disk transient plane source method under controlled air pressure conditions. (a) Sketch of the set up. (b) Optical image of the vacuum desiccator and hot disk sample holder.

Compressive strain was incrementally applied to the fabric samples (Figure 3.2) to study the effect of deformation on the out-of-plane thermal conductivity. During compression, the fiber volume fraction increased, which induced a rise in the volumetric heat capacity of the system. Although the heat capacity per unit mass of the fabric was approximately that of the solid, the same did not apply for the heat capacity per unit volume since the volume of air represented 55-70% of the RVE volume, see Figure 3.3 (f). Subsequently, thermal conductivity measurements were corrected at each loading

condition. This study shows that, to make this correction, it is possible to use the fiber volume fraction computed in compression by FEA, because direct measurement is not feasible experimentally. It can be argued that the compression strain in experiment differs from the computational result. For this reason, the bridge between experiment and model is done through the compression stress, calculated from the applied transverse load in the experiment and reaction force in the model. It is assumed that both experiment and model will produce the same deformation state under an equal compression stress. Therefore, for each measurement, the volume fraction is calculated computationally from the deformation state (% Compression strain in Figures 3.3 (e) and (f)) that yields the stress value measured in the experiment.

To study the effect of air pressure in the thermal conduction of the fabric, the sample holder was mounted inside a vacuum cabinet (F42400-4021, Bel-Art SP Scienceware, NJ, USA) (Figure 3.2 (b)), (29inHg vacuum for 72hr capacity). Hi-Nicalon and heat-cleaned Nextel-BF20 samples were tested under the same conditions. A sensor of 6.4 mm radius was used to perform the measurements. To prevent air leaks, epoxy resin was used to seal the cable of the hot-disk sensor. A ply of 4 fabric samples was used at each side of the sensor. The optimum recording time and output power were determined through an iterative process. A transient recording time of 10s and an output power of 40 mW were used in this study for both materials. Starting from an un-loaded state, the thermal conductivity was measured at 1 and 0.16 atm before an increase in compressive stress, 3 thermal conductivity measurements were executed for each data point. To ensure the

system returned to thermal equilibrium and mechanical relaxation, wait times of 30 minutes were used between measurements. Room temperature conditions remained constant at 23 ± 1 C.

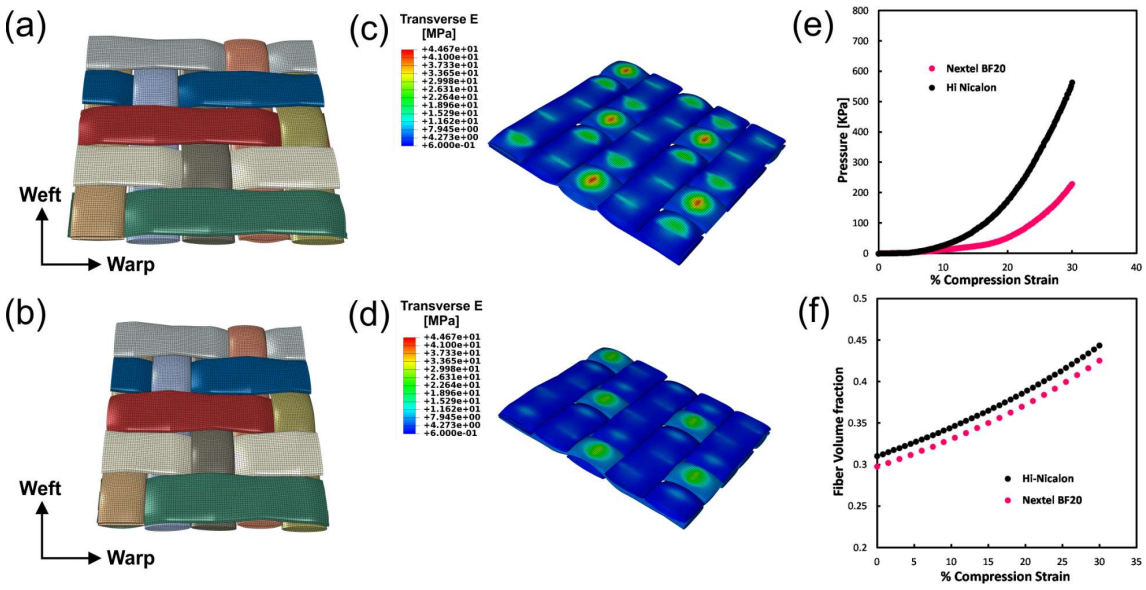

Figure 3.3: Representative Volume Element (RVE) mechanical model. (a) Hi-Nicalon 5HS woven fabric RVE. (b) Nextel-BF20 woven fabric RVE. (c) Transverse Young's modulus map of Hi-Nicalon at 30% compression strain. (d) Transverse Young's modulus map of Nextel-BF20 at 30% compression strain. (e) Mechanical compression pressure as function of compression strain for Hi-Nicalon and Nextel-BF20. (f) Fiber volume fraction of the RVE as a function of compression strain for Hi-Nicalon and Nextel-BF20.

3.3 Computational finite element modeling

3.3.1 Woven fabric modeling and mechanical behavior

Due to their periodic structure, Nextel-BF20 and Hi-Nicalon fabrics were modeled with a minimum representative volume element (RVE) as shown in Figure 3.3 (a) and (b),

respectively. Their geometry was determined by scanning electron microscopy (SEM). The geometry of the RVE was generated using the software TEXGEN [24] and the finite element models were produced following the methodology described in Section 2.4.

Hi-Nicalon 5HS was found to be a well-balanced fabric, with the same amount of fiber count per unit length in the warp and weft directions. The dimensions of the RVE before compression were 5 x 5 x 0.5 mm^3. By contrast, Nextel-BF20 was found to be a non-balanced fabric. Although the nominal count of fibers per yarn was the same for the warp and weft directions, the count per unit length was different, because of the yarns compressed in the warp direction as shown in Figure 3.3 (b). The dimensions of the RVE before compression were 4.15 x 5 x 0.55 mm^3.

As discussed in Section 2.4, the mechanical constitutive law developed by Lin et al. [25] was used, this law allows for the Young's modulus of the yarn in the transverse direction to increase with compression strain, due to an increase in local volume fraction.

A 30% compression strain simulation was performed for both models. Figure 3.3 (e) shows the evolution of compressive stress as a function of applied compressive strain. The Hi-Nicalon model exhibited a higher increase in compressive stress after an 8% strain than Nextel, reaching a pressure of 563.5 KPa at the end of the simulation. The pressure in the Nextel model evolved at a slower pace to reach 229.7 KPa. Figures 3.3 (c) and (d) show the local transverse Young's modulus through the geometry of the RVEs at 30% compression. Both models exhibited stiffening on the spots where the yarns are woven.

The Nextel RVE produced a bigger overall Young's modulus through the warp yarns when compared to the weft yarns. No major difference in stiffness was found between weft and warp yarns for the Hi-Nicalon RVE.

The variation of volume fraction in the RVE with compression was determined under the assumption that the total volume of fibers remained constant through the compression.

As discussed in Section 3.2, only the compression stress was measured during the hot-disk experiment. The volume fractions used to revise the volumetric heat capacity were obtained by mapping the reaction loads in the simulation and experiment. Each experimental measurement was performed at a compression stress, these values were mapped to the computational compression strain in Figure 3.3 (e) and then the volume fraction was extracted from the relation shown in Figure 3.3 (f).

From the mechanical compression simulation, the mean yarn volume fraction was found to vary between 0.4748 and 0.5327 for the Hi-Nicalon model, and between 0.4933 and 0.5183 for the Nextel-BF20 model.

3.3.2 Micro level intra-yarn model

To accurately represent the thermal conduction at the microscale, in the yarns, the commonly used series formulation was substituted by a 3D finite element model of the

fibrous structure. SEM analysis of the yarn structure (Figure 3.1 (c) and (d)), indicated that the fibers were mostly parallel to each other with a random cross-sectional distribution. RVEs with periodic boundaries were built with V_{fiber} = 45, 50, 55 and 60% following this hypothesis.

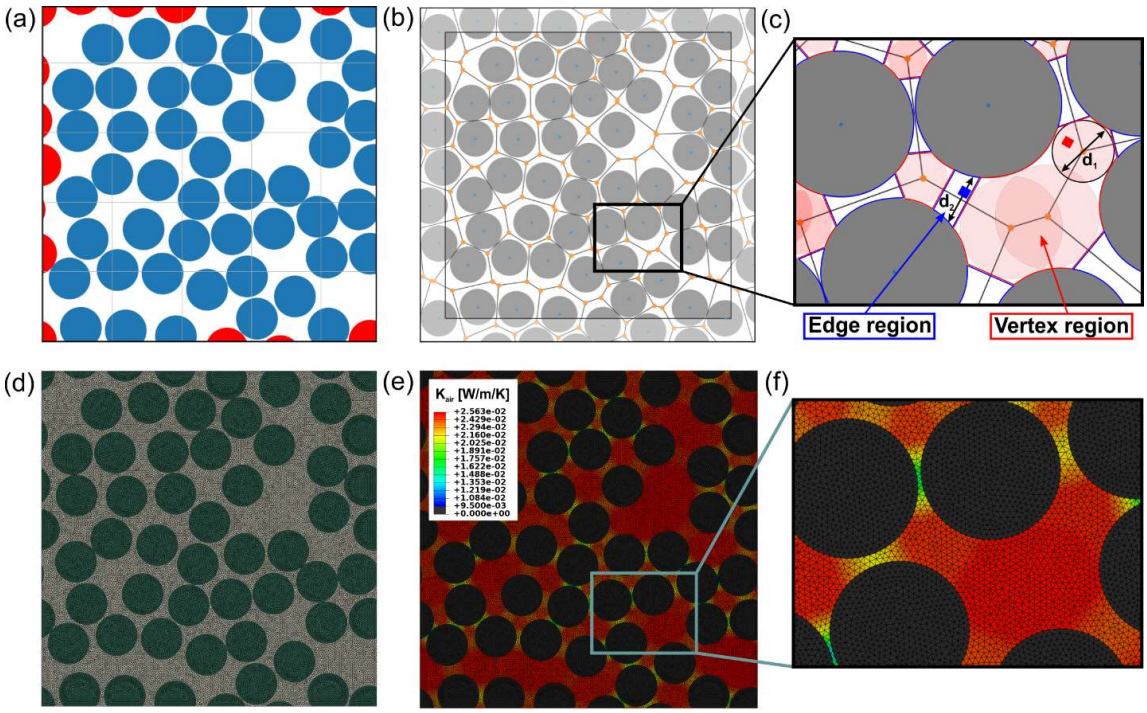

Figure 3.4: Intra-yarn Representative Volume Element (RVE) thermal modeling. (a) Randomized periodic structure of fibers. (b) Voronoi cell structure of the RVE and (c) gap size method for local assignment of thermal conductivities. (d) Finite element mesh of the intra-yarn RVE. (e) Air thermal conductivity map of the periodic RVE, and (f) close view of the intra-yarn thermal conductivity map.

A Discrete Element Method (DEM) solver was coded to generate the fiber distributions (Figure 3.4). A set of 49 fibers with a prescribed radius were located in the plane with a square packing structure. The fibers were positioned at equidistance to produce the prescribed volume fraction. The elements (fibers) were given random forces

and the simulation box boundaries were set to periodic. A penalty contact property was stablished between them and the simulation was left to run to produce a random distribution. Figure 3.4 (a) shows the result of this simulation, in blue the simulated fibers, in red the periodic counterparts inside the simulation box. The fiber distribution was imported to ABAQUS [26] afterwards and meshed. Diffusive tetrahedral elements were used with a size of 0.5 μm. The Hi-Nicalon fibers and Nextel-440 fibers were modeled using cylinders with a diameter D_f = 14 μm, and 12 μm, respectively. The space occupied by air was modeled as a fluid matrix.

It has been shown that to improve the description of the thermal behavior in confined air in micro spacings, as a function of pressure and temperature, the air thermal conductivity K_{air} must be corrected as [3],

$$K_{air} = \frac{K_{air0}}{1 + 2\frac{(2-\alpha)2\gamma}{\alpha(\gamma+1)}\frac{1}{Pr}Kn} \tag{3.3}$$

where K_{air0} is the thermal conductivity of free air, α is an accommodation coefficient that characterizes the behavior of a gas particle in the collisions with a solid and varies between 0 and 1 [3], $\gamma = C_p/C_v$ is the adiabatic coefficient or heat capacity ratio, Pr is the Prandtl number and Kn is the Knudsen number, given by the expression:

$$Kn = \frac{\lambda}{L_c} = \frac{K_B T}{\pi\sqrt{2}{d_g}^2 P L_c} \tag{3.4}$$

Here, λ is the molecular mean free path length, K_B is Boltzmann's constant, T is the gas temperature, d_g is the diameter of the gas molecule, P is the pressure, and L_c is the characteristic length.

The Knudsen number is defined as the ratio between the molecular mean free path length of a gas to a characteristic physical length and indicates whether the gas can be considered a continuum or kinetics theory of gases should be applied. When the characteristic length approaches the molecular mean free path and $Kn > 0.1$, continuum theory is no longer applicable, and the thermal conductivity should be corrected by using Equation 3.3 [3].

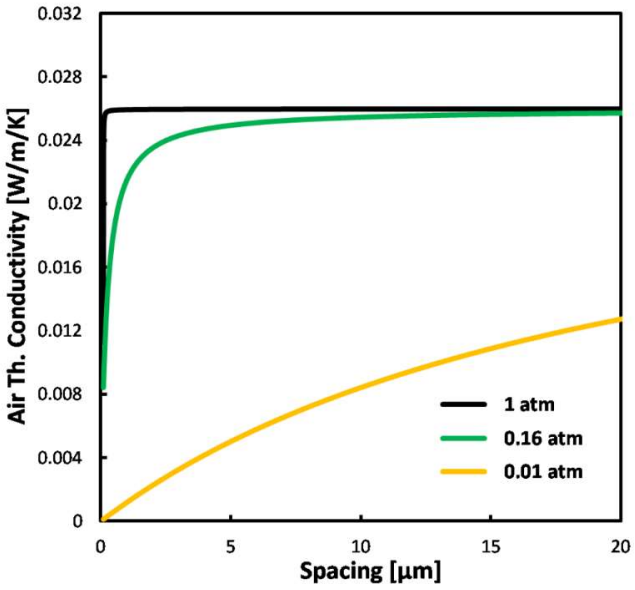

Figure 3.5: Thermal conductivity of air as a function of confinement spacing for an air pressure of 1, 0.16 and 0.01 atm.

Figure 3.5 shows the value of air thermal conductivity as a function of spacing or characteristic length value, for different pressure values.

The characteristic length L_c for fibrous insulations is typically approximated by the characteristic pore length as [12],

$$L_c = \frac{\pi D_f}{4V_f} \tag{3.5}$$

To properly assign a conductivity value to air elements according to their L_c, the air region was spatially parametrized using a Voronoi cell structure as shown in Figure 3.4 (b). On each Voronoi vertex, a pore space was defined as the largest circle, centered at the vertex, without fiber material (Figure 3.4 (c)). A characteristic length (L_c) equal to the diameter of the circle was assigned to the pore. The air space was divided in 2 region types: "vertex" region (red in Figure 3.4 (c)) was the space where the pores covered the Voronoi cell boundaries, and "edge" region (blue in Figure 3.4 (c)) the remaining space within fibers. If an air element centroid was in the "vertex" region, the thermal conductivity was calculated using the characteristic length of the pore that contained the element (d_1 in Figure 3.4 (c)), the largest characteristic length if it lied in more than one pore, and the characteristic length of the closest pore if it was not contained by any pore. On the other hand, if an element centroid was in the "edge" region, L_c was calculated as the length of the line, perpendicular to the Voronoi cell boundary, that goes through the centroid of the element and connects both fibers (d_2 in Figure 3.4 (c)). The thermal conductivity was then

computed for all the air elements in the RVE, the resulting model accounted for micro-spacing effects in between fibers as well as any variation in pressure as shown in Figures 3.4 (e) and (f).

A 296 K predefined temperature field was established as initial condition. A temperature gradient of 5 K was applied as the boundary condition, keeping the rest of the surfaces insulated. Due to the low temperatures and low gradients, radiation effects were considered negligible. Air was considered stagnant within the porous structure, therefore only thermal transport through conduction was contemplated.

Material properties were modeled by heat-transfer user-defined material subroutines (UMATHT) in ABAQUS. The thermal conductivities of the fibers were those estimated from experiments, as discussed above. Air thermal conductivity properties were calculated for pressures of 1 atm, 0.16 atm and 0.01 atm using Equations 3.3 and 3.4.

The steady-state heat conduction was calculated using Fourier's law:

$$Q = -K_{eff} A \frac{\Delta T}{\Delta x} \tag{3.6}$$

where Q is the computed heat flow, K_{eff} is the effective thermal conductivity, A was the cross-sectional area of the RVE, ΔT was the temperature gradient, and Δx was the dimension of the RVE.

Two RVE structures were made for each volume fraction. Each structure was run twice, with the temperature gradient placed in the vertical and horizontal directions. A total of 4 simulations per volume fraction were computed and the final K_{eff} value was averaged. An exponential curve was fitted to get an expression for the transverse thermal conductivity as a function of volume fraction.

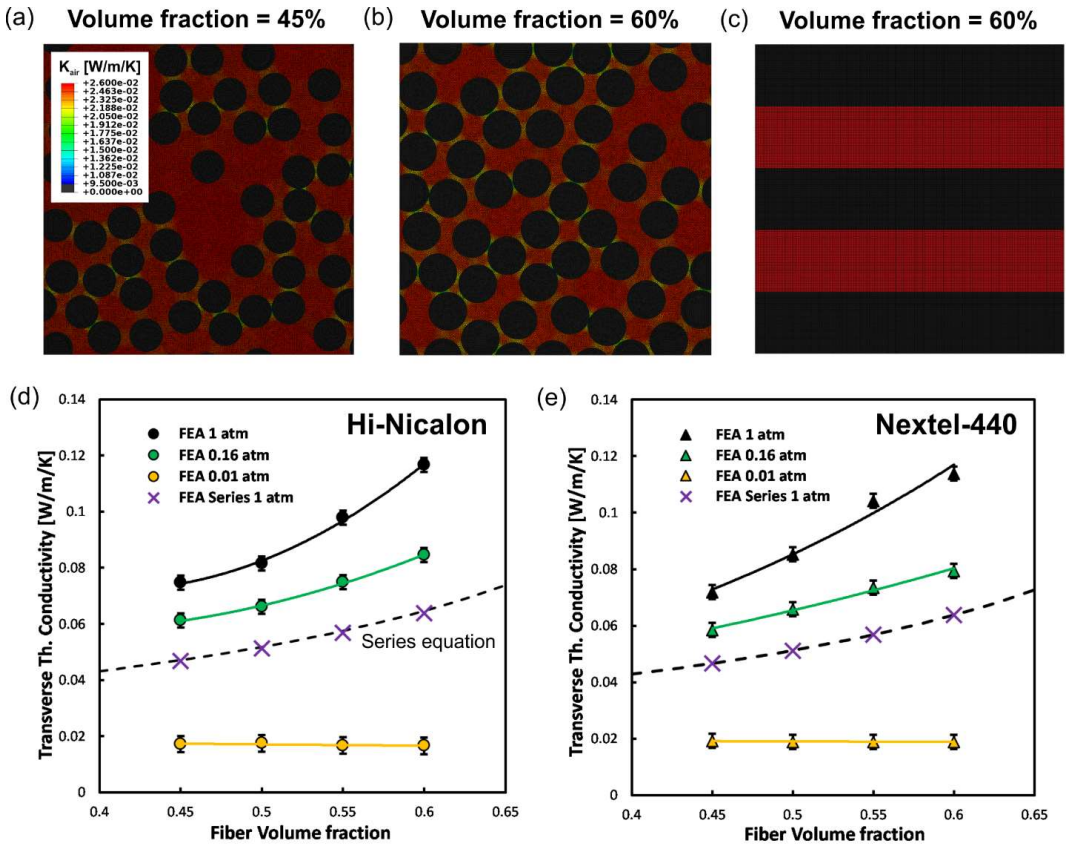

Figure 3.6: Intra-yarn steady-state heat transfer finite element analysis. (a)-(b) RVE models of a Hi-Nicalon yarn with 45 and 60% volume of fiber, respectively. (c) Pure series finite element model. (d) Simulated transverse thermal conductivity of a Hi-Nicalon yarn as a function of fiber volume fraction. (e) Simulated transverse thermal conductivity of a Nextel-440 yarn as a function of fiber volume fraction. The dashed black lines represent the solution of the series model equation for confined air at 1 atm.

A second type of model, resembling the series model formulation (Figure 3.6 (c)) was created for comparison. In this geometry, air thermal conductivity was given by Equations 3.3, 3.4 and 3.5. Boundary conditions, element type, step and property extraction remained unaltered.

3.3.3 Woven fabric equilibrium heat-transfer simulation

A steady-state heat transfer simulation was performed at every 1.5% compression over the fabric RVE following the methodology described in Section 2.4.3. Two heat transfer constitutive models were used to describe the thermal behavior of the yarn. In the first one, the series model was used together with Equations 3.3, 3.4 and 3.5, i.e. the black dashed lines in Figures 3.6 (d) and (e). The second one used a multiscale approach, here the transverse effective thermal conductivity of the yarn was given by the micro-scale yarn simulation results in Figure 3.6. The longitudinal thermal conductivity of the yarn is given by combination of the parallel model and Equations 3.3, 3.4 and 3.5. The material behavior was implemented using a user material subroutine UMATHT.

The air within the yarn structure was modeled with a gap thermal conductance property, this surface-to-surface element interaction was defined as:

$$Cond = \frac{K_{air}}{L_c} \tag{3.7}$$

where K_{air} is given by Equation 3.3, and L_c is the gap size. The evolution of the gap thermal conductance property as a function of gap size is shown in Figure 3.7.

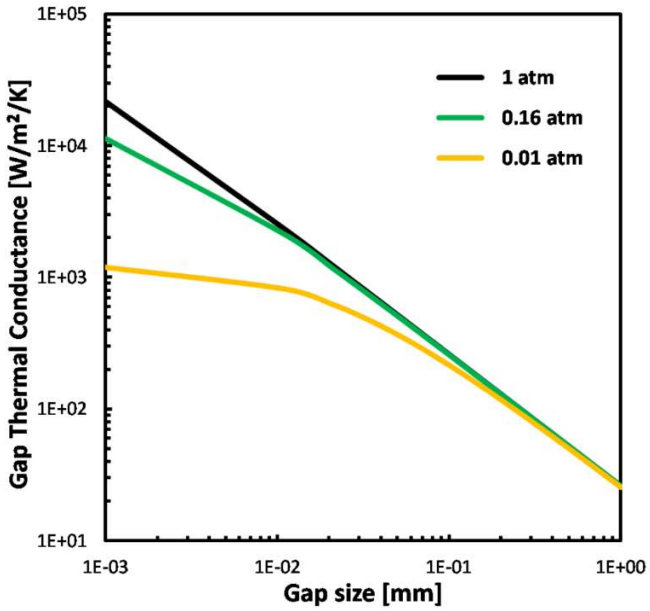

Figure 3.7: Thermal conductance of air as a function of confinement spacing for an air pressure of 1, 0.16 and 0.01 atm

3.4 Computational heat-transfer results

3.4.1 Simulated yarn transverse thermal conductivity

As described above, microscopic level yarn models were generated for various volume fractions of fiber and their effective thermal conductivity was simulated by steady-state heat-transfer FEA in both Hi-Nicalon and Nextel-440 yarns at different gas pressures. Figure 3.6 (a) and (b) show the thermal conductivity map for a Hi-Nicalon yarn at 1 atm

with a fiber volume fraction of 45 and 60% respectively. Figure 3.6 (c) shows the FEA series model for Hi-Nicalon at 1 atm and a fiber volume fraction of 60%, for comparison.

The results for Hi-Nicalon and Nextel-440 models are presented in Figures 3.6 (d) and (e) respectively. The black dashed line represents the solution to the series formulation together with Equations 3.3, 3.4 and 3.5 at 1 atm. Our FEA series model gave the same solution. Interestingly, however, the series solution is smaller than the new thermal conductivity with the proposed microscale yarn model for 1 atm. The dependency on the volume fraction is also observed to be more pronounced, the series model increases the conductivity by 35% with a change in fiber volume fraction from 45 to 60%, while the proposed model reacts with a 55% increase in conductivity for Hi-Nicalon and a 60% increase for the Nextel-440 model. The volume fraction dependency appears to have a more linear behavior for the Nextel model.

Furthermore, the thermal conductivity increase with fiber volume fraction softens as pressure is decreased. A reduction between 15% and 20% is observed for a fiber volume fraction of 45% when pressure changes from 1 atm to 0.16 atm, while a drop of 25 to 30% is observed for a fiber volume fraction of 60%. For these pressure conditions, the spacing dependency of air thermal conductivity for the micro-scale is already significant as we can see in Figure 3.5. For an air pressure of 0.01 atm, we find that the model predicts a transverse thermal conductivity almost constant of 0.017 W/m/K, a reduction by almost an order of magnitude with respect to that in the 1 atm model.

The difference in the response of the model to a variation of fiber thermal conductivity was found to be negligible. The model results, however, reveal a higher sensitivity to slight changes of fiber diameter (14μm in Hi-Nicalon to 12μm in Nextel-440). For the range of thermal conductivities and length scales that are presented in this study, the model response is primarily controlled by the geometry and air thermal properties. The standard deviation for the models is found to be lower than 0.003 W/m/K.

Figures 3.8 (a) and (b) show the effect of vacuum pressure on the local air thermal conductivity for a Nextel-440 yarn with a fiber volume fraction of 45% and 60%, respectively. At 1 atm most of the pore structure (vertex regions) conserve a thermal conductivity close to that of free air (0.026 W/m/K), the effect of air confinement is only relevant for narrow edge regions were fibers are almost in contact. At 0.16 atm all edge regions display a significant drop in thermal conductivity, while thermal conductivity in vertex regions are still relatively high, especially in those with a high characteristic length. For the 0.01 atm case we can observe that the computed thermal conductivity in the edge regions is an order of magnitude lower compared to that of free air. The vertex regions suffer now a general significant decrease in thermal conductivity. By comparison of Figures 3.8 (a) and (b), we can observe that the effect of increasing the volume fraction can be described as an increase in edge regions in detriment of the amount and size of vertex regions. Thus, the increase in fiber volume fraction has a lower effect on the overall thermal

conductivity as the vacuum level increases, this is the effect depicted in Figure 3.6 (d) and (e).

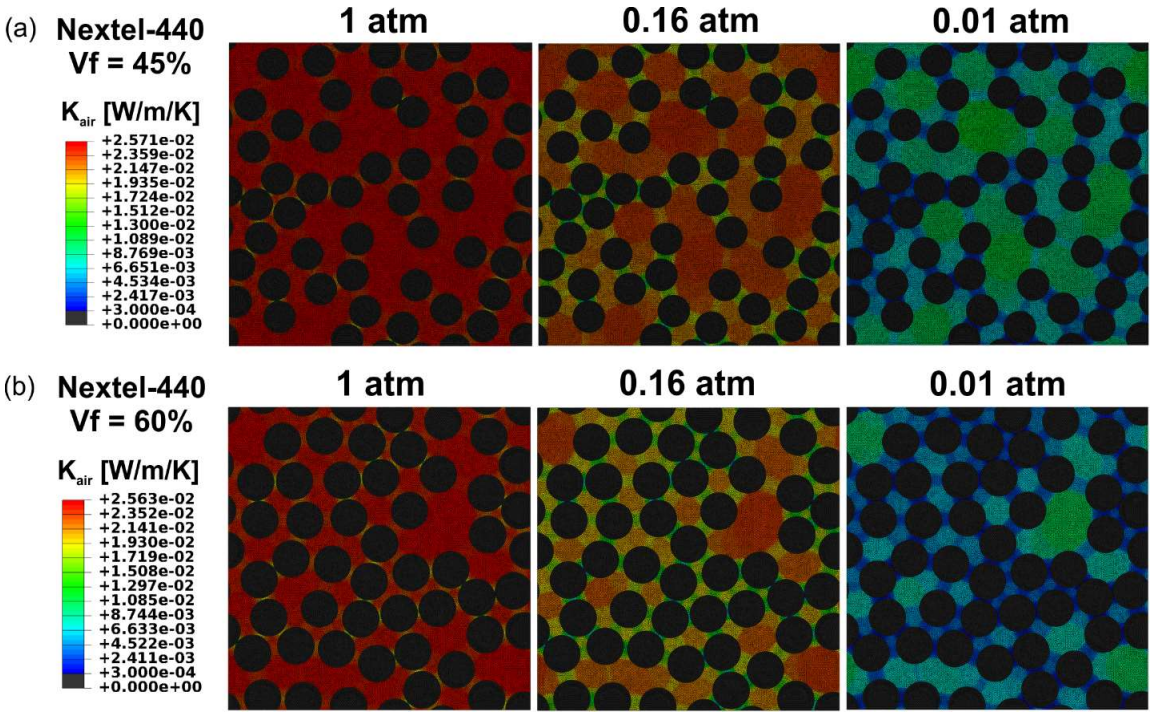

Figure 3.8: Nextel-440 intra-yarn model air thermal conductivity maps for an air pressure of 1, 0.16 and 0.01 atm for: (a) yarn with 45% fiber volume fraction, and (b) yarn with 60% fiber volume fraction.

Figures 3.9 (a) and (b) show the effect of vacuum over the local heat flux for a Nextel-440 yarn as a function of fiber volume fraction. We can observe that, for 1 atm, the heat finds preferential paths through the fibers and edge regions in the direction of the temperature gradient (vertical) as the volume fraction rises, promoting the increase in effective thermal conductivity shown in Figure 3.6 (e). As seen in Figure 3.8, although the conductivity drops in the narrow edge regions this reduction is not enough to counter the effect of the fibers getting closer (thermal conductivity 2 orders of magnitude higher), so

the preferential paths form. On the other hand, for 0.01 we observe that the heat flux remains uniform as the volume fraction rises. The reduction from 1 atm to 0.01 atm greatly increases the effect of micro-spacing confinement as Figure 3.5 shows. All edge regions have now a small thermal conductivity value as shown in Figure 3.8. Consequently, as volume fraction rises, the heat flux finds a big resistance to form those preferential paths that appear for 1 atm. Therefore, air thermal conductivity for a pressure of 0.01 atm, strongly controls the behavior of the model. Hi-Nicalon exhibits the exact same behavior.

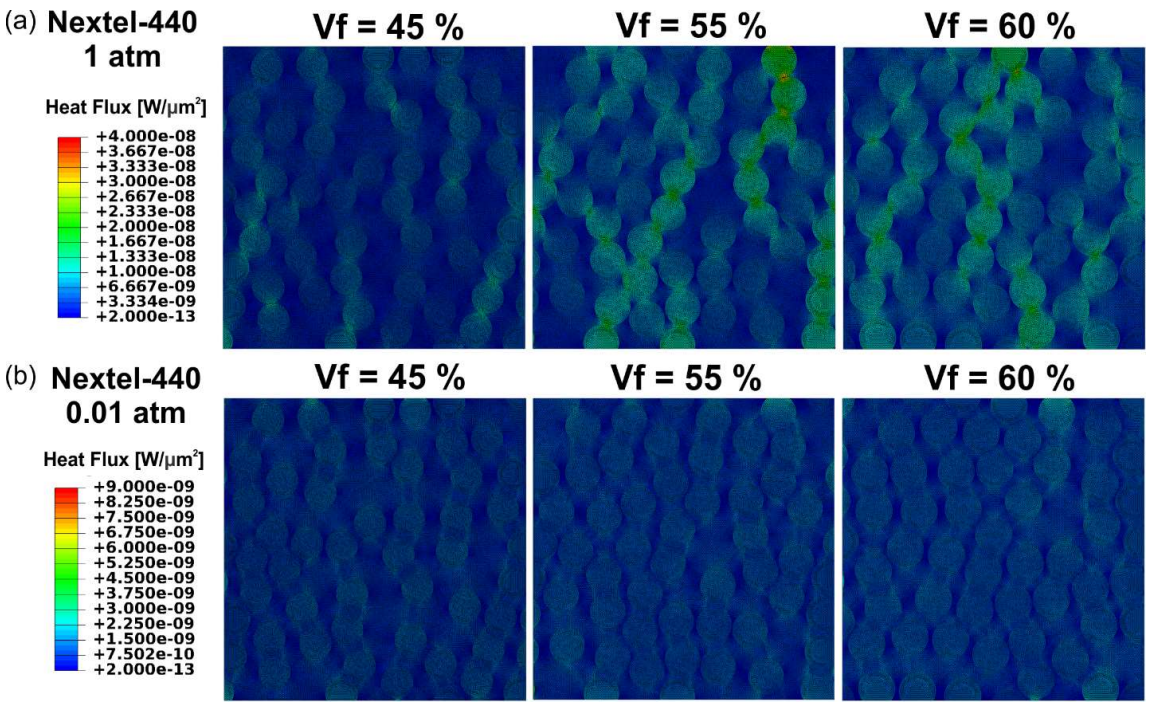

Figure 3.9: Nextel-440 intra-yarn model heat flux maps for a volume fraction of 45, 55 and 60% at different air pressure: (a) 1 atm, and (b) 0.01 atm.

3.4.2 Woven fabric out-of-plane thermal conductivity results

Figures 3.10 (a) and (b) show the comparison between the transient plane source measurements and the out-of-plane finite-element results. It can be observed that the proposed multiscale computational approach successfully captures the effect of compressive stress and atmospheric pressure over the fabric out-of-plane thermal conductivity, for both types of fabrics.

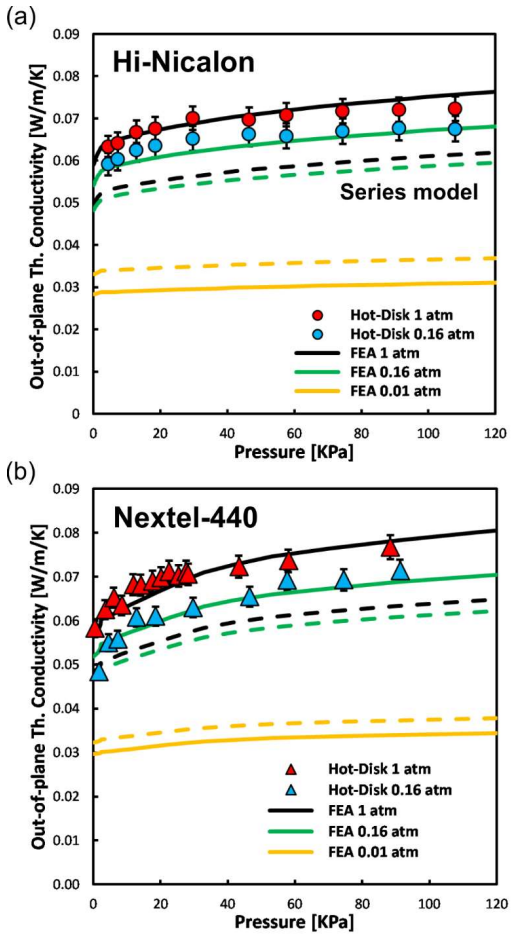

Figure 3.10: Simulated out-of-plane thermal conductivity compared to the hot-disk transient plane source measurements under compressive strain, for (a) Hi-Nicalon 5HS fabric and (b) Nextel-BF20 fabric. The dashed lines represent the simulation results using the series model for the transverse thermal conductivity of the yarn

Furthermore, Figure 3.10 shows that the series model (dashed lines) does not produce an accurate result. The computational results from the series model underestimate the effective thermal conductivity compared to the multiscale approach for 1 and 0.16 atm. However, for 0.01 atm it overestimates the value. This indicates that modelling the yarn as resistances placed in series and averaging the pore size as shown in Equation 3.5 is not an effective solution to capture the thermal behavior of woven fabrics under different air pressures.

Qualitatively, by focusing on the shape of the curves and the evolution of the measurements with compressive stress, we observe that the Hi-Nicalon fabric evolves differently than Nextel-BF20. The Nextel fabric shows 3 distinguishable regimes: a sudden jump in conductivity in the beginning of the curve that was associated to a jump-to-contact in the yarns during compression, a second regime were conductivity increases due to gaps closing and yarn densification, and a third region after 30KPa with a softer increase in conductivity where all that is observed is densification of the yarns. This is further explained in Chapter 2 (these 3 regimes are present for all the studied vacuum levels). Hi-Nicalon on the other hand, does not show that second transition. After the gap overclosure at the beginning, the conductivity increases with no sudden changes in slope. The more regular and balanced structure of the Hi-Nicalon 5HS fabric may promote this behavior.

3.5 Discussion

3.5.1 Effect of gas pressure in the out-of-plane thermal conductivity of woven fabrics

Out-of-plane thermal conductivity in woven fabrics is clearly influenced by gas pressure as we can see in Figure 3.10, both computationally and experimentally. The Knudsen correction to the gas conductivity described by Equation 3.3 is demonstrated to be essential to understand this behavior. Figures 3.5 and 3.7 show the dependency of thermal conductivity and thermal conductance, respectively, on the gas pressure for stagnant air in micro-spacing. The immediate consequence of this behavior is clearly observed in Figure 3.8 showing that the change in pressure dramatically affects the air thermal conductivity, especially in the edge regions where the characteristic length is smaller. In observing Figures 3.8 and 3.9 together, it can be understood how the Knudsen effect controls the heat transfer through conduction inside the yarns. By lowering the gas pressure, the mean free path of the air molecules increases while the characteristic length of the confinement remains the same or even is reduced with compressive strain. Consequently, the gas not only reduces its conductivity through the entire porous structure, but also large resistances form in the edge regions, preventing the heat to find a preferential path. A similar effect should be expected in yarn-to-yarn contacts.

3.5.2 Multiscale approach versus series formulation

Figure 3.10 provides clear evidence that the multiscale approach proposed in this study perfectly captures the behavior and magnitude of the experimental measurements, as opposed to the commonly used series model. Although the latter qualitatively captures the trend and shape of the curve, it fails to predict the magnitude for all vacuum levels tested. This result is important in different aspects. First, the series arrangement of a group of resistances or conductances represent the lower bound of effective overall conductivity for the system, while the parallel arrangement is the upper bound. Therefore, in the series model (Figure 3.6 (c)), it is assumed that the heat flux through the system is homogeneous with no preferential path and must go through the air. A concrete example to understand the importance of the preferential path is revealed in Figure 3.9. As explained in the previous section, the heat flux increases with volume fraction at 1 atm because preferential paths are found, on the contrary at 0.01 atm the same increase in volume fraction does not produce an increase in heat flux. As the real structure of a yarn clearly has networks of preferential heat paths, the series formulation will always underestimate the value.

Second, the series formulation cannot properly capture the geometry of the system. To implement the Knudsen effect into the series model, a value of the characteristic length as a function of fiber volume fraction is used as described by Equation 3.5. Consequently, a constant pore size is being used, which neglects the effects of high thermal resistances that appear on the edge regions.

Finally, the multiscale formulation allows for further implementation of physical phenomena such as oxidation or phase changes in the fiber material or the study of thermal contact resistances. The effect of thermal contact resistances should increase for volume fractions closer to a square packing, due to the increase in fiber-to-fiber contacts, and play a determinant role for ultra-high vacuum levels where conduction through the fibrous network and thermal radiation are the main heat carriers. Here, heat constriction resistances would limit the heat flow through the network [27].

3.5.3 Out-of-plane thermal conductivity difference between Nextel-BF20 and Hi-Nicalon

From Figures 3.10 (a) and (b), 6 (d) and (e) we observe that the overall out-of-plane behavior of Hi-Nicalon and Nextel-BF20 at room temperature are similar. The thermal conductivity of the fibers are close, 8 W/m/K for Hi-Nicalon and an approximate range of 5 to 7 W/m/K for Nextel-440 fibers. Although both bulk silicon carbide and alumina have much higher conductivity [23,28], the nanocrystalline structure of Hi-Nicalon [23] and the silicon oxide and glassy faces present in Nextel fibers [14] makes these values to drop by an order of magnitude.

As noted in Section 3.4.2, Nextel-BF20 develops a dependency on compression stress that slightly differs to that of Hi-Nicalon. Hi-Nicalon does not show a sudden transition in slope for thermal conductivity growth as compression stress increases. This effect is attributed to the more regular and balanced geometrical structure of Hi-Nicalon.

The Nextel-440 yarn model did not exhibit a significant change when the conductivity of the fiber was set from 7 to 5 W/m/K, which suggests that the few differences in magnitude between the Hi-Nicalon yarn and the Nextel yarn are driven by the geometry.

3.5.4 Limitations of the model

As explained in Section 2.4, to be able to perform the mechanical compression step, the air matrix elements around the yarn were removed and substituted by a gap thermal conductance property (Figure 3.7). This property is a surface-to-surface contact interaction that works well between close-to-parallel surface meshes but are not guaranteed to be reliable otherwise. This, together with the suppression of air elements in the in-plane boundaries of the RVE, prevented us to correctly apply the necessary boundary conditions and output requests to compute the effective in-plane thermal conductivity by FEA. The use of conjugate heat-transfer methods [29-31] may be able to solve this problem.

Furthermore, at the yarn level, assuming a perfect parallel arrangement of fibers may be overestimating the longitudinal value in the same fashion that the series model underestimates the transverse value.

3.6 Conclusions

A multiscale thermo-mechanical FEA model was created to simulate and study the evolution of the out-of-plane thermal conductivity with different strain and gas pressures in 2D woven ceramic fabric materials. Nextel-BF20 and Hi-Nicalon 5HS fabric materials were modeled and their thermal conductivity was computed, as a function of compressive stress, for air pressures between 1, 0.16 and 0.01 atm. The results were validated through experimental measurements at 1 and 0.16 atm using the hot-disk transient plane source technique. The following major conclusions can be drawn from the present study:

- The out-of-plane thermal conductivity in 2D woven fabric materials decreases with the increase in vacuum level due to Knudsen effects in micro-spacings. We observe that not only the magnitude is reduced but the dependency on compression stress falls as pressure drops. This is attributed to a pronounced decrease in air conductivity in the spacing between fibers that prevents the formation of preferential heat flow paths as the volume fraction increases.

- The FEA multiscale approach proposed and the transient plane source measurements showed excellent agreement for both Nextel-BF20 and Hi-Nicalon fabrics. The series formulation for transverse yarn thermal conductivity, however, produces inaccurate results. This suggests that a proper geometry at the micro-level, inside the yarn, is essential to accurately capture the behavior of the material in the meso-level.

This study shows that by applying the proposed methodology, the out-of-plane thermal conductivity of woven fabrics under compressive stress and at different gas pressures, can be accurately modelled. The addition of the microscale model allows for the use of non-isotropic fiber properties and other complex phenomena. The proposed modeling technique could be adapted to more complex loading cases and different woven materials and is of interest for flexible TPS applications.

References

[1] R. Penide-Fernandez, F. Sansoz, Anisotropic thermal conductivity under compression in two-dimensional woven ceramic fibers for flexible thermal protection systems, Int. J. Heat Mass Transf, 145 (2019) 118721.

[2] J. Del Corso, F. Cheatwood, W. Bruce, S. Hughes, A. Calomino, Advanced high-temperature flexible TPS for inflatable aerodynamic decelerators, 21st AIAA Aerodyn, Decelerator Syst. Technol. Conf. Semin. (2011) 1–23.

[3] M.G. Kaganer, Israel Program for Scientific Translations, Thermal Insulation in Cryogenic Engineering (1969)

[4] M. Bahrami, M.M. Yovanovich, J.R. Culham, Effective thermal conductivity of rough spherical packed beds, Int. J. Heat Mass Transf. 49 (2006) 3691–3701.

[5] J. Kwon, C.H. Jang, H. Jung, T. Song, Effective thermal conductivity of various filling materials for vacuum insulation panels, Int. J. Heat Mass Transf, 52 (23–24) (2009) 5525-5532

[6] J.J. Zhao, Y.Y. Duan, X.D. Wang, B.X. Wang, Effects of solid-gas coupling and pore and particle microstructures on the effective gaseous thermal conductivity in aerogels, J. Nanoparticle Res. 14 (8) (2012) 1024.

[7] D.S. Smith, A. Alzina, J. Bourret, B. Nait-Ali, F. Pennec, N. Tessier-Doyen, K. Otsu, H. Matsubara, P. Elser, U.T. Gonzenbach, Thermal conductivity of porous materials, J. Mater. Res. 28 (2013) 2260–2272

[8] A. Das, R. Alagirusamy, P. Kumar, Study of heat transfer through multilayer clothing assemblies: A, 11 (2011) 54–60.

[9] M. Fu, M.Q. Yuan, W.G. Weng, Modeling of heat and moisture transfer within firefighter protective clothing with the moisture absorption of thermal radiation, Int. J. Therm. Sci., 96 (2015) 201-210

[10] K. Daryabeigi, Thermal Analysis and Design of Multi-layer Insulation for Re- entry Aerodynamic Heating, in: 35th AIAA Thermophysics Conference 11-14 June 2001 Anaheim, Aerospace, 2001, pp. 1–8.

[11] K. Daryabeigi, G.R. Cunnington, S.D. Miller, J.R. Knutson, Combined Heat Transfer in High-Porosity High-Temperature Fibrous Insulations: Theory and Experimental Validation, J. Thermophys. Heat Tr., 25 (2011) 536-546

[12] S. Yuan Zhao, B. Ming Zhang, X. Dong He, Temperature and pressure dependent effective thermal conductivity of fibrous insulation, Int. J. Therm. Sci. 48 (2) (2009) 440–448.

[13] S.A. Lurie, Y.O. Solyaev, D.V. Lizunova, L.N. Rabinskiy, V.M. Bouznik, O. Menshykov, Influence of mean distance between fibers on the effective gas thermal conductivity in highly porous fibrous materials. Int. J. Heat Mass Transf, 109 (2017) 511-519.

[14] Duan Li, Bin Li, Yuanyi Zheng, Shitao Gao, Xuejin Yang, On the mechanical, thermophysical and dielectric properties of Nextel™ 440 fiber reinforced nitride matrix (N440/Nitride) composites, Ceramics International, 44 (6) (2018) 6137-6143

[15] E.L. Christiansen, B. Alan Davis, Heat-Cleaned Nextel in MMOD Shielding, First Int'l. Orbital Debris Conf, (2019) Conference Paper

[16] D.J. Duval, S.H. Risbud, J.F. Shackelford, Mullite, (2008).

[17] D. Schawaller, B. Clauß, M.R. Buchmeiser, Ceramic filament fibers - A review, Macromol. Mater. Eng. 297 (2012) 502–522.

[18] R. Yamada, N. Igawa, T. Taguchi, S. Jitsukawa, Highly thermal conductive, sintered SiC fiber-reinforced 3D-SiC/SiC composites: experiments and finite-element analysis of the thermal diffusivity/conductivity, Journal of Nuclear Materials, 307–311 (2) (2002) 1215-1220,

[19] Y. He, Rapid thermal conductivity measurement with a hot disk sensor: Part 1. Theoretical considerations, Thermochim. Acta. 436 (1) (2005) 122–129.

[20] S.E. Gustafsson, Transient plane source techniques for thermal conductivity and thermal diffusivity measurements of solid materials, Rev. Sci. Instrum. 62 (1991) 797–804.

[21] M. Gustavsson, H. Nagai, T. Okutani, Characterization of anisotropic and irregularly shaped materials by high-sensitive thermal conductivity measurements, Solid State Phenom. 124–126 (2007) 1641–1644.

[22] N.K. Michael, G. Miller, Jason M. Keith, Julia A. King, Brian J. Edwards, Measuring thermal conductivities of anisotropic synthetic graphite-liquid crystal polymer composites, Polym. Compos. 27 (4) (2006) 388–394.

[23] B. Zhu, R. Wang, S. Harrison, K. Williams, R. Goduguchinta, J. Schneiter, J. Pegna, E. Vaaler, X. Wang, Thermal conductivity of SiC microwires: Effect of

temperature and structural domain size uncovered by 0 K limit phonon scattering, Ceram. Int. 44 (2018) 11218–11224.

[24] H. Lin, L.P. Brown, A.C. Long, Modelling and Simulating Textile Structures Using TexGen, Adv. Mater. Res. 331 (2011) 44–47.

[25] H. Lin, M. Sherburn, J. Crookston, A.C. Long, M.J. Clifford, I.A. Jones, Finite element modelling of fabric compression, Model. Simul. Mater. Sci. Eng. 16 (3) (2008).

[26] ABAQUS 2018, Dassault Systèmes Simulia Corp., Johnston, RI, USA, 2017

[27] Chuan-Yong Zhu, Zeng-Yao Li, Modeling of the apparent solid thermal conductivity of aerogel, Int. J. Heat Mass Transf. 120 (2018) 724-730

[28] P. Auerkari, Mechanical and physical properties of engineering alumina ceramics, Technical Research Centre of Finland, VTT Manufacturing Technology, Research Notes 1792 (1996) 3-36.

[29] D.J. Lopez Penha, S. Stolz, J.G.M. Kuerten, M. Nordlund, A.K. Kuczaj, B.J. Geurts, Fully-developed conjugate heat transfer in porous media with uniform heating, Int. J. Heat Fluid Flow. 38 (2012) 94–106.

[30] J. Ross-Jones, M. Gaedtke, S. Sonnick, M. Rädle, H. Nirschl, M.J. Krause, Conjugate heat transfer through nano scale porous media to optimize vacuum insulation panels with lattice Boltzmann methods, Comput. Math. with Appl. 77 (2019) 209–221.

[31] A.G. Fedorov, R. Viskanta, Three-dimensional conjugate heat transfer in the microchannel heat sink for electronic packaging, Int. J. Heat Mass Transf. 43 (2000) 399–415.

CHAPTER 4: SUMMARY AND FUTURE WORK

4.1 Major conclusions

Thermo-mechanical modeling of high temperature woven ceramic materials is central for accurate thermal analysis of flexible TPS in harsh environments. The complex porous structure of these materials has been proven to greatly affect heat conduction. Multiscale thermo-mechanical finite element models of 2D woven Hi-Nicalon SiC fibers and alumina-based Nextel-440, with a 5-harness satin weave pattern, were created to study heat conduction through the fabrics, under transverse loading, at different gas pressures. In parallel, an experimental methodology was developed to validate the computational results, by using the anisotropic transient plane source method at room temperature.

The proposed multiscale modeling approach was limited in its capability to accurately predict thermal conductivity of fabrics in the in-plane direction.

Both experimental and computational results show that, at an air pressure of 1 atm and ambient room temperature, the thermal conductivity in 2D woven ceramic fabrics increases under compressive stress. Computationally we discovered that, this effect is caused primarily by gap overclosure between yarns and densification of fibers within them during compression, establishing a relationship between the increase of effective thermal conductivity with fiber volume fraction. As a result of the constitutive description of the yarn, in the transverse direction, the Young's modulus of the yarn elements increases with transverse loading, simulating an increase in local fiber volume fraction. This fiber

densification produces the effective thermal conductivity increase after the yarn gap overclosure stage.

The faster relative increase of thermal conductivity in the out-of-plane direction with respect to the in-plane resulted in a change in thermal conductivity anisotropy. Anisotropy was observed to decrease at 1 atm and room temperature with compressive stress.

At the micro level, confined gas within a porous structure has been shown to play a central role in the thermal conductivity of the material. When the molecular mean free path of a gas approaches the characteristic length of its confinement space, the gas experiences a reduction in thermal conductivity that is known as Knudsen effect. For a porous material as a woven ceramic fabric and a given interstitial gas, Knudsen effects appear when, (1) the gas pressure is reduced, (2) the characteristic length of the confinement shrinks, or (3) a combination of both. A micro level model of the fiber arrangement within the yarn was created to study the consequences of the Knudsen effect in the porous structure and to accurately capture the behavior of the out-of-plane thermal conductivity during transverse mechanical loading. Gas pressures of 1, 0.16 and 0.01 atm were studied computationally. However, only measurements at 1 atm and 0.16 atm were taken.

Nextel-BF20 and Hi-Nicalon samples were tested with the transient plane source method under vacuum. The experimental results showed a decrease in the out-of-plane thermal conductivity. Computationally, the multiscale approach allowed to study the behavior at the micro-level, which the transient plane source method is not capable of.

In the mesoscale, aside from the decrease in thermal conductivity, a decline in the dependency on compression stress was observed. At the microscale, for 1 atm, the transverse thermal conductivity increases as fiber volume fraction increases, because of the formation of preferential heat flow paths in the direction of the temperature gradient. However, when pressure was decreased, air thermal conductivity suffers a net decrease as a consequence of Knudsen's effects. It was shown that this decrease, especially in the narrow areas within 2 fibers (edge regions), prevents the formation of preferential heat flow paths as the fiber volume fraction increases, finally leading to the decrease in compression stress dependency.

The presented multiscale approach was tested against the commonly used series formulation for the transverse behavior of a yarn. When compared to the experimental measurements, the multiscale approach showed excellent agreement for both Nextel-BF20 and Hi-Nicalon, while the series formulation underestimated the thermal conductivity value for 1 and 0.16 atm. The multiscale approach proved to surpass the series model simulating the behavior of the woven fabric material.

4.2 Future research

Through the course of this research, the author has encountered multiple areas and topics that are of great interest as next steps for further development of this project. This section presents some ideas for future studies.

4.2.1 Experimental studies

Radiation, Rosseland mean extinction coefficient.

To study the thermal conduction of materials at high temperature, especially after 700K [1], heat conduction through radiation must be included. For optically thick media, such as the 2D woven ceramic fabrics, radiation through the material can be considered as a diffusion process [2], so the radiative heat flux can be expressed as:

$$q_r = -\frac{16n^2\sigma}{3k_r}T^3\frac{\delta T}{\delta x} \tag{4.1}$$

so, the thermal conductivity through radiation is:

$$K_{rad} = \frac{16}{3}n^2\frac{\sigma}{k_r}T^3 \tag{4.2}$$

where n is the index of refraction, σ is Stefan-Boltzmann constant, T is the temperature and k_r the Rosseland mean extinction coefficient, that represents the overall effect of energy decay in the material [2]. To characterize k_r it is necessary to measure the spectral

transmittances in the wavelength range of 2.5-25 μm through the studied range of temperatures (note that the effect of K_{rad} raises quickly with temperature), this can be accomplished using a Fourier Transform Infrared Spectrometer [2, 3].

However, it has been shown that this thermal diffusive process through fibrous media is orientation dependent [4], so K_{rad} becomes an orientation-dependent temperature-dependent tensor.

The diffusion approximation allows us to sum the radiation contribution to the gas and solid contributions of thermal conductivity. Thus, given that the developed model has a coordinate system attached to each element, the tensor K_{rad} can be added directly to the UMATHT subroutine controlling the yarn behavior.

Hot-Disk measurements with other interstitial gases.

The methodology developed in this dissertation enables the testing of thermal properties for different gases. Other gases such as He, CO_2 or Ar, with thermal conductivities of 0.1557, 0.0168 and 0.0177 W/m/K respectively [5-8], could be introduced to the vacuum cabinet using a 3-way valve.

High-vacuum and high-temperature Hot-Disk measurements.

The Hot-disk transient plane source method has proved to be an excellent option for thermal property characterization of fibrous insulation. To further proceed with the

validation process of the computational advancements to implement in the current finite-element model, further capabilities of testing will be necessary. The two main open fronts are:

- Pure solid conduction through contact points plays a bigger role in the overall thermal conductivity the lower the gas pressure. To validate a pure-solid conductivity model, a high vacuum hot-disk (or other thermal analysis method) may be required.

- Thermal conductivity at high temperatures, as discussed previously, has a notable contribution on heat transfer through radiation. To validate any modeling involving high temperature, measurements of thermal conductivity as a function of temperature are necessary.

4.2.2 Computational studies

Silicon carbide oxidation rate by reactive force field atomistic simulations

In the study of thermo-mechanical behavior of ceramic fabric materials, phase changes and formation of other components play a notable role [9].

Unlike Nextel-440 fibers that are already an oxide, Hi-Nicalon fibers suffer an oxidation process [10]:

$$SiC + 3/2\, O_2 \rightarrow SiO_2 + CO \tag{4.3}$$

Reactive force field potentials for atomistic simulations have proven capable of reproducing these phenomena [11]. The atomistic study of oxidation could provide an oxidation rate through an Arrhenius law that can be then coded inside the constitutive thermal model (UMATHT) of the fibers in future heat transfer transient analysis of the fabric material.

Contact Mechanics. Solid network thermal conductivity

In the study of thermal behavior of fibrous materials under high vacuum levels, relevant for the applications discussed in this work, solid thermal conductivity plays a big role. Some studies [2,12,13] use empirically fit or simplified models to describe the effect of thermal contacts over the fibrous network. However, to properly model the behavior through solid contacts, constriction/spreading resistance must be also considered [14-18]. For high vacuum and low temperatures, heat-flow gets forced to go through solid contacts. However, this means that the contacts may act as bottlenecks for heat flow [14-17] (Figure 4.1). Analogously to what happens with Knudsen effects in confined gasses, when the true contact radius of the contact approaches the phonon mean free path the heat transfer is ballistic. On the contrary, if the true contact area is in much larger than phonon mean free path the heat transfer is in diffusive limit and the constriction resistance (in a sphere-sphere) is approximated by [17]:

$$R_{cd} = \frac{1}{2K_{spher}\ a} \tag{4.4}$$

where a is the radius of the contact area and K_{sphere} is the thermal conductivity of the solid material. This formulation could be easily implemented into finite element contact properties once it is well characterized for the fiber geometry and real contact area. A refinement of the microscale model to account for contact within fibers without losing the air elements to simulate Knudsen's effect is necessary.

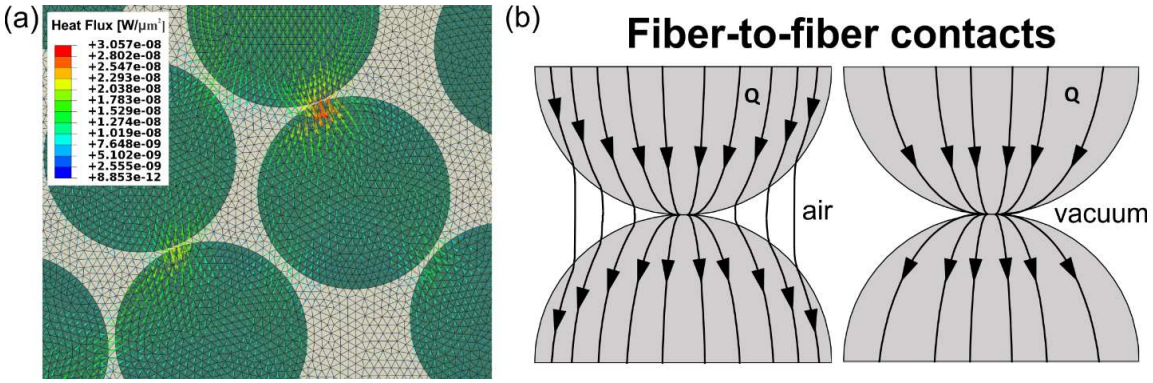

Figure 4.1: Heat flux vector field between fibers. (a) Heat flux vector field in the current model at 1 atm, no contact. (b) Heat flux vector field schematic for fiber-to-fiber contacts

Conjugate heat-transfer coupling. Coherent Mesh. In-plane thermal conductivity

Although Conjugate Heat-Tansfer (CHT) corresponds to the combination of heat transfer in solids and fluids, the computational results presented in this research have been

all produced by finite element modeling, both air and solid materials were given conductivity and specific heat values and were solved using the FEA formulation. To account for a proper behavior of the fluid part, a co-simulation technique involving computational solid mechanics and computational fluid dynamics is necessary. This would allow for a proper fluid-solid interaction solving transient problems.

A related issue to solve here is to create a coherent mesh for both solid and fluid, that allows the fabric structure to perform dynamics problems (compression, shear, etc.) without giving up on the capability of simulating fluid heat transfer. This would solve the problem for the in-plane thermal conductivity prediction.

Micro-level yarn modeling. Fiber properties and longitudinal model

The microlevel model presented in this research has been used to properly understand the transverse behavior of a yarn, by changing fiber arrangement, fiber volume fraction, and air pressure. However, the air property formulation admits changes on temperature through the constitutive law, and an analogous constitutive law can be programmed for the fiber material to change the element properties as a function of temperature (or even time). Oxidation rates, material phase changes etc. could be added to the model through here. Once these models are developed, the behavior can be coded into the yarn material subroutine.

Thermal behavior with different gases.

As noted in Section 4.2.1, the thermal conductivity of woven fabrics could be measured, with different interstitial gases, by using the Hot-Disk transient plane source method. The use of different gases for the thermal modeling of the multiscale structure involves changing the gas conductivity and gas conductance property through Equation 3.3.

Fully coupled thermal-mechanical FEA constitutive model

The current model presents a Non-coupled thermo-mechanical model, meaning that dynamics and heat transfer are solved separately. Once the previously described computational problems are solved and tested, a comprehensive material constitutive model that couples thermal and mechanical behavior should be coded.

References

[1] T.M. Tritt, Kluwer Academic/Plenum Publishers, Thermal Conductivity, (2004).

[2] S. Yuan Zhao, B. Ming Zhang, X. Dong He, Temperature and pressure dependent effective thermal conductivity of fibrous insulation, Int. J. Therm. Sci. 48 (2009) 440–448.

[3] J. Yang, Y. Zhang, Z. Hong, R. Ma, D. Zhang, X. Wang, C. Sun, Z. Hu, Preparations of TiO2 nanocrystal coating layers with various morphologies on Mullite fibers for infrared opacifier application, Thin Solid Films, 520 (2012) 2651–2655.

[4] S.C. Lee, Effect of fiber orientation fibrous on thermal radiation media in fibrous media, Int J. Heat and Mass Transfer, 32 (2) (1989) 311–319.

[5] E. Vogel, B. Jäger, R. Hellmann, E. Bich, Ab initio Pair Potential Energy Curve for the Argon Atom Pair and Thermophysical Properties for the Dilute Argon Gas. II. Thermophysical Properties for LowDensity Argon, Mol. Phys. 108 (2010) 3335-3352.

[6] E. F. May, R. F. Berg, M. R. Moldover, Reference Viscosities of H2, CH4, Ar, and Xe at Low Densities, Int. J. Thermophys. 28 (2007) 1085–1110.

[7] W. Cencek, J. Komasa, M. Przybytek, J. B. Mehl, B. Jeziorski, K. Szalewicz, Effects of Adiabatic, Relativistic, and Quantum Electrodynamics Interactions in Helium Dimer on Thermophysical Properties of Helium, J. Chem. Phys., 136, 224303 (2012).

[8] V. Vesovic, W. A. Wakeham, G. A. Olchowy, J. V. Sengers, J. T. R.Watson, J. Millat, The Transport Properties of Carbon Dioxide, J. Phys. Chem. Ref. Data, 19 (3) (1990) 763-808.

[9] W. Owens, D. Merkel, F. Sansoz, D. Fletcher, Fracture behavior of woven silicon carbide fibers exposed to high-temperature nitrogen and oxygen plasmas, J. Am. Ceram. Soc. 98 (2015) 4003–4009.

[10] D. Schawaller, B. Clauß, M.R. Buchmeiser, Ceramic filament fibers - A review, Macromol. Mater. Eng. 297 (2012) 502–522.

[11] D. a. Newsome, D. Sengupta, H. Foroutan, M.F. Russo, A.C.T. van Duin, Oxidation of Silicon Carbide by O2 and H2O: A ReaxFF Reactive Molecular Dynamics Study, Part I, J. Phys. Chem. C. 116 (2012) 16111–16121.

[12] K. Daryabeigi, AIAA 2001-2834 Thermal Analysis and Design of Multi-layer Insulation for Re-entry Aerodynamic Heating. 35th AIAA Thermophysics Conference Anaheim, Aerospace. (2001).

[13] J.S. Kwon, C.H. Jang, H. Jung, T.H. Song, Effective thermal conductivity of various filling materials for vacuum insulation panels, Int. J. Heat Mass Transf. 52 (2009) 5525–5532.

[14] D. Singh, J.Y. Murthy, T.S. Fisher, Phonon transport across mesoscopic constrictions, J. Heat Transfer. 133 (2011) 1–8.

[15] G.R. McGree, M.H. Schankula, M.M. Yovanovich Thermal resistance of cylinder-flat contacts: theoretical analysis and experimental verification of a line-contact model, Nuclear Engineering and Design 86 (1985) 369-381.

[16] M. Bahrami, M.M. Yovanovich, J.R. Culham, Effective thermal conductivity of rough spherical packed beds, Int. J. Heat Mass Transf. 49 (2006) 3691–3701.

[17] C.Y. Zhu, Z.Y. Li, Modeling of the apparent solid thermal conductivity of aerogel, Int. J. Heat Mass Transf. 120 (2018) 724-730.

[18] T. Kek-Kiong, S.S. Sadhal, Thermal constriction resistance: effects of boundary conditions and contact geometries, Int. J. Heat Mass Transf. 35 (1992) 1533–1544.

BIBLIOGRAPHY

ABAQUS 2018, Dassault Systèmes Simulia Corp., Johnston, RI, USA, 2017

Abdel-Rehim, M.M. Saad, M. El-Shakankery, I. Hanafy, Textile fabrics as thermal insulators, Autex Res. J. 6 (3) (2006) 148–161.

Arambakam, H. Vahedi Tafreshi, B. Pourdeyhimi, A simple simulation method for designing fibrous insulation materials, Mater. Des. 44 (2013) 99–106.

Arambakam, H. Vahedi Tafreshi, B. Pourdeyhimi, Modeling performance of multi-component fibrous insulations against conductive and radiative heat transfer, Int. J. Heat Mass Transf. 71 (2014) 341–348.

Auerkari, Mechanical and physical properties of engineering alumina ceramics, Technical Research Centre of Finland, VTT Manufacturing Technology, Research Notes 1792 (1996) 3-36.

Bahrami, M.M. Yovanovich, J.R. Culham, Effective thermal conductivity of rough spherical packed beds, Int. J. Heat Mass Transf. 49 (2006) 3691–3701.

Bascom and S. Wong, The friction and wear of TPS fibers, Progress report on NASA grant NAG 2-444. (1987)

Baxter, The thermal conductivity of textiles, Proc. Phys. Soc. 58 (1) (1946) 105–118.

Bejan, Heat Transfer Handbook, Wiley-Interscience, (2003)

Bogaty, N.R.S. Hollies, M. Harris, Some Thermal Properties of Fabrics: Part I: The Effect of Fiber Arrangement, Text. Res. J. 27 (6) (1957) 445–449.

Bunsell, Oxide fibers for high-temperature reinforcement and insulation, Jom. 57 (2005) 48–51.

Cencek, J. Komasa, M. Przybytek, J. B. Mehl, B. Jeziorski, K. Szalewicz, Effects of Adiabatic, Relativistic, and Quantum Electrodynamics Interactions in Helium Dimer on Thermophysical Properties of Helium, J. Chem. Phys., 136, 224303 (2012)

Christiansen, B. Alan Davis, Heat-Cleaned Nextel in MMOD Shielding, First Int'l. Orbital Debris Conf, (2019) Conference Paper

COMSOL Multiphysics®. www.comsol.com. COMSOL AB, Stockholm, Sweden

Daryabeigi, AIAA 2001-2834 Thermal Analysis and Design of Multi-layer Insulation for Re-entry Aerodynamic Heating. 35th AIAA Thermophysics Conference Anaheim, Aerospace. (2001).

Daryabeigi, G.R. Cunnington, S.D. Miller, J.R. Knutson, Combined Heat Transfer in High-Porosity High-Temperature Fibrous Insulations: Theory and Experimental Validation, J. Thermophys. Heat Tr., 25 (2011) 536-546

Das, R. Alagirusamy, P. Kumar, Study of heat transfer through multilayer clothing assemblies: A, 11 (2011) 54–60.

Dasgupta, R.K. Agarwal, S.M. Bhandarkar, Three-dimensional modeling of woven-fabric composites for effective thermo-mechanical and thermal properties, Compos. Sci. Technol. 56 (3) (1996) 209–223.

Del Corso, F. Cheatwood, W. Bruce, S. Hughes, A. Calomino, Advanced High-Temperature Flexible TPS for Inflatable Aerodynamic Decelerators, 21st AIAA Aerodyn. Decelerator Syst. Technol. Conf. Semin. (2011) 1–23.

Del Corso, Walter E. Bruce, III, Stephen J. Hughes, John A. Dec, Marc D. Rezin, and F.M.C. B. Meador, Haiquan Guo, Douglas G. Fletcher, Anthony M. Calomino, Flexible Thermal Protection System Development for Hypersonic Inflatable Aerodynamic Decelerators 9 Th International Planetary Probe Workshop, (2012).

Dixit, H.S. Mali, R.K. Misra, Unit cell model of woven fabric textile composite for multiscale analysis, Procedia Eng., Elsevier B.V. 68 (2013) 352–358.

Duval, S.H. Risbud, J.F. Shackelford, Mullite, (2008).

Fedorov, R. Viskanta, Three-dimensional conjugate heat transfer in the microchannel heat sink for electronic packaging, Int. J. Heat Mass Transf. 43 (2000) 399–415.

Fu, M.Q. Yuan, W.G. Weng, Modeling of heat and moisture transfer within firefighter protective clothing with the moisture absorption of thermal radiation, Int. J. Therm. Sci., 96 (2015) 201-210

Fukushima, Y. Yoshizawa, Journal of the European Ceramic Society Fabrication and morphology control of highly porous mullite thermal insulators prepared by gelation freezing route, J. Eur. Ceram. Soc. 36 (2016) 2947–2953.

Gong, Y. Wang, X. Cheng, R. Zhang, H. Zhang, Porous mullite ceramics with low thermal conductivity prepared by foaming and starch consolidation, J. Porous Mater. 21 (1) (2014) 15–21.

Gustafsson, Transient plane source techniques for thermal conductivity and thermal diffusivity measurements of solid materials, Rev. Sci. Instrum. 62 (1991) 797–804.

Gustavsson, Specific heat measurements with the hot disk thermal constants analyser. Thermal Conductivity 23 (1996) 56-65.

Gustavsson, H. Nagai, T. Okutani, Characterization of anisotropic and irregularly-shaped materials by high-sensitive thermal conductivity measurements, Solid State Phenomena 124-126 (2007) 1641-1644.

He, Rapid thermal conductivity measurement with a hot disk sensor: Part 1. Theoretical considerations, Thermochim. Acta. 436 (1) (2005) 122–129.

Hill, R.D. Braun, Modeling of Plain Woven Fabrics for Inflatable Aerodynamic Decelerators, 55th AIAA/ASME/ASCE/AHS/ASC Structures, Structural Dynamics, and Materials Conference (2014) 1–12.

Hughes, J.S. Ware, J.A.D. Corso, R.A. Lugo, Deployable aeroshell flexible thermal protection system testing, 20th AIAA Aerodyn. Decelerator Syst. Technol. Conf. (2009) 1–21.

Ishikawa, Recent developments of the SiC fiber Nicalon and its composites, including properties of the SiC fiber Hi-Nicalon for ultra-high temperature, Compos. Sci. Technol. 51 (1994) 135–144.

Ismail, A.S. Ammar, M. El-Okeily, 4. Heat transfer through textile fabrics: mathematical model, Appl. Math. Model. 12 (4) (1988) 434–440.

Jirsak, T. Gok, B. Ozipek, N. Pan, Comparing Dynamic and Static Methods for Measuring Thermal Conductive Properties of Textiles, Text. Res. J. 68 (1) (1998) 47–56.

Kaganer, Israel Program for Scientific Translations, Thermal Insulation in Cryogenic Engineering (1969)

Kek-Kiong, S.S. Sadhal, Thermal constriction resistance: effects of boundary conditions and contact geometries, Int. J. Heat Mass Transf. 35 (1992) 1533–1544.

Kwon, C.H. Jang, H. Jung, T. Song, Effective thermal conductivity of various filling materials for vacuum insulation panels, Int. J. Heat Mass Transf, 52 (23–24) (2009) 5525-5532

Lee, Effect of fiber orientation fibrous on thermal radiation media in fibrous media, Int J. Heat and Mass Transfer, 32 (2) (1989) 311–319.

Li, S. Li, Y. Wang, Prediction of effective thermal conductivities of woven fabric composites using unit cells at multiple length scales, J. Mater. Res. 26 (3) (2011) 384–394.

Li, Bin Li, Yuanyi Zheng, Shitao Gao, Xuejin Yang, On the mechanical, thermophysical and dielectric properties of Nextel™ 440 fiber reinforced nitride matrix (N440/Nitride) composites, Ceramics International, 44 (6) (2018) 6137-6143

Lin, L.P. Brown, A.C. Long, Modelling and Simulating Textile Structures Using TexGen, Adv. Mater. Res. 331 (2011) 44–47. http://texgen.sourceforge.net

Lin, M.J. Clifford, A.C. Long, M. Sherburn, Finite element modelling of fabric shear, Model. Simul. Mater. Sci. Eng. 17 (1) (2009).

Lin, M. Sherburn, J. Crookston, A.C. Long, M.J. Clifford, I.A. Jones, Finite element modelling of fabric compression, Model. Simul. Mater. Sci. Eng. 16 (3) (2008).

Lopez Penha, S. Stolz, J.G.M. Kuerten, M. Nordlund, A.K. Kuczaj, B.J. Geurts, Fully-developed conjugate heat transfer in porous media with uniform heating, Int. J. Heat Fluid Flow. 38 (2012) 94–106.

Lurie, Y.O. Solyaev, D.V. Lizunova, L.N. Rabinskiy, V.M. Bouznik, O. Menshykov, Influence of mean distance between fibers on the effective gas thermal conductivity in highly porous fibrous materials. Int. J. Heat Mass Transf, 109 (2017) 511-519.

Maqsood, M. Anis-Ur-Rehman, V. Gumen, Anwar-Ul-Haq, Thermal conductivity of ceramic fibres as a function of temperature and press load, J. Phys. D. Appl. Phys. 33 (16) (2000) 2057–2063.

Martin, L. College, G.E.R. Lamb, Measurement of Thermal Conductivity of Nonwovens Using a Dynamic Method, Text. Res. J. 57 (12) (1987) 721–727.

Martin, Geometric and Mechanical Modelling of Textiles. PhD thesis, University of Nottingham, Nottingham, UK (2007).

May, R. F. Berg, M. R. Moldover, Reference Viscosities of H2, CH4, Ar, and Xe at Low Densities, Int. J. Thermophys. 28 (2007) 1085–1110.

McGree, M.H. Schankula, M.M. Yovanovich Thermal resistance of cylinder-flat contacts: theoretical analysis and experimental verification of a line-contact model, Nuclear Engineering and Design 86 (1985) 369-381.

Michael G. Miller, Jason M. Keith, Julia A. King, Brian J. Edwards, Measuring Thermal Conductivities of Anisotropic Synthetic Graphite–Liquid Crystal Polymer Composites, Polymer composites 27 (4) (2006): 388-394.

Mohammadi, P. Banks-Lee, P. Ghadimi, Determining Effective Thermal Conductivity of Multilayered Nonwoven Fabrics, Text. Res. J. 73 (9) (2003) 802–808.

Montgomery, Viscosity and Thermal Conductivity of Air and Diffusivity of Water Vapor in Air, J. Meteor. 4 (1947) 193-196.

Newsome, D. Sengupta, H. Foroutan, M.F. Russo, A.C.T. van Duin, Oxidation of Silicon Carbide by O2 and H2O: A ReaxFF Reactive Molecular Dynamics Study, Part I, J. Phys. Chem. C. 116 (2012) 16111–16121.

Ning, T. Chou, A general analytical model for predicting the transverse effective thermal conductivities of woven fabric composites, Construction. (97) (1998) 315–322.

Ning, T.-W. Chou, Closed-form solutions of the in-plane effective thermal conductivities of woven-fabric composites, Compos. Sci. Technol. 55 (1) (1995) 41–48.

Owens, Aero-Thermal Characterization of Silicon Carbide Flexible Tps Using a 30Kw Icp Torch, University of Vermont, 2015.

Owens, D. Merkel, F. Sansoz, D. Fletcher, Fracture Behavior of Woven Silicon Carbide Fibers Exposed to High-Temperature Nitrogen and Oxygen Plasmas, J. Am. Ceram. Soc. 98 (2015) 4003–4009.

Penide-Fernandez, F. Sansoz, Anisotropic thermal conductivity under compression in two-dimensional woven ceramic fibers for flexible thermal protection systems, Int. J. Heat Mass Transf, 145 (2019) 118721.

Pradère, J.M. Goyhénèche, J.C. Batsale, S. Dilhaire, R. Pailler, Thermal diffusivity measurements on a single fiber with microscale diameter at very high temperature, Int. J. Therm. Sci. 45 (5) (2006) 443–451.

Ross-Jones, M. Gaedtke, S. Sonnick, M. Rädle, H. Nirschl, M.J. Krause, Conjugate heat transfer through nano scale porous media to optimize vacuum insulation panels with lattice Boltzmann methods, Comput. Math. with Appl. 77 (2019) 209–221.

T.O.F. Contents, Journal of the European Ceramic Society, J. Eur. Ceram. Soc. Artic. Press. (2013) 1–11.

Tritt, Kluwer Academic/Plenum Publishers, Thermal Conductivity, (2004).

Schawaller, B. Claußß, M.R. Buchmeiser, Ceramic filament fibers - A review, Macromol. Mater. Eng. 297 (2012) 502–522.

Siddiqui, D. Sun, Finite element analysis of thermal conductivity and thermal resistance behaviour of woven fabric, Comput. Mater. Sci. 75 (2013) 45–51.

Singh, J.Y. Murthy, T.S. Fisher, Phonon transport across mesoscopic constrictions, J. Heat Transfer. 133 (2011) 1–8.

Smith, A. Alzina, J. Bourret, B. Nait-Ali, F. Pennec, N. Tessier-Doyen, K. Otsu, H. Matsubara, P. Elser, U.T. Gonzenbach, Thermal conductivity of porous materials, J. Mater. Res. 28 (2013) 2260–2272.

Urano, A Saeki, M Takeda, A Yokoyama, Oxidative degradation behavior of polycarbosilane-derived silicon carbide fibers, Ceram. Eng. Sci. Proc., 20 (3) (1999) 85.

Vesovic, W. A. Wakeham, G. A. Olchowy, J. V. Sengers, J. T. R.Watson, J. Millat, The Transport Properties of Carbon Dioxide, J. Phys. Chem. Ref. Data, 19 (3) (1990) 763-808.

Villière, D. Lecointe, V. Sobotka, N. Boyard, D. Delaunay, Experimental determination and modeling of thermal conductivity tensor of carbon/epoxy composite, Compos. Part A Appl. Sci. Manuf. 46 (1) (2013) 60–68.

Vogel, B. Jäger, R. Hellmann, E. Bich, Ab initio Pair Potential Energy Curve for the Argon Atom Pair and Thermophysical Properties for the Dilute Argon Gas. II. Thermophysical Properties for LowDensity Argon, Mol. Phys. 108 (2010) 3335-3352.

WiseTex, S.V. Lomov, I. Verpoest, E. Bernal, F. Boust, V. Carvelli, J. Delerue, … F. Tümer, Virtual Textile Composites Software WiseTex: Integration with Micro-mechanical, Permeability and Structural Analyses." Fifteenth International Conference on Composite Materials 65 (15-16) (2005) 2563-2574. https://www.mtm.kuleuven.be/Onderzoek/Composites/software/ wisetex

Wu, G. Shao, X. Shen, S. Cui, L. Wang, Novel Al_2O_3–SiO_2 composite aerogels with high specific surface area at elevated temperatures with different alumina/silica molar ratios prepared by a non-alkoxide sol–gel method, RSC Advances, 6 (2016) 5611-5620.

Yamada, N. Igawa, T. Taguchi, S. Jitsukawa, Highly thermal conductive, sintered SiC fiber-reinforced 3D-SiC/SiC composites: experiments and finite-element analysis of the thermal diffusivity/conductivity, Journal of Nuclear Materials, 307–311 (2) (2002) 1215-1220.

Yang, Y. Zhang, Z. Hong, R. Ma, D. Zhang, X. Wang, C. Sun, Z. Hu, Preparations of TiO2 nanocrystal coating layers with various morphologies on Mullite fibers for infrared opacifier application, Thin Solid Films, 520 (2012) 2651–2655.

Zhao, Y.Y. Duan, X.D. Wang, B.X. Wang, Effects of solid-gas coupling and pore and particle microstructures on the effective gaseous thermal conductivity in aerogels, J. Nanoparticle Res. 14 (8) (2012) 1024.

Zhao, B. Ming Zhang, X. Dong He, Temperature and pressure dependent effective thermal conductivity of fibrous insulation, Int. J. Therm. Sci. 48 (2) (2009) 440–448.

Zhu, R. Wang, S. Harrison, K. Williams, R. Goduguchinta, J. Schneiter, J. Pegna, E. Vaaler, X. Wang, Thermal conductivity of SiC microwires: Effect of temperature and structural domain size uncovered by 0 K limit phonon scattering, Ceram. Int. 44 (2018) 11218–11224.

Zhu, Zeng-Yao Li, Modeling of the apparent solid thermal conductivity of aerogel, Int. J. Heat Mass Transf. 120 (2018) 724-730.